Environmental Modelling and Software 185 (2025) 106270

Contents lists available at ScienceDirect

Environmental Modelling and Software

journal homepage: www.elsevier.com/locate/envsoft

Position Paper

A coupled multiscale description of seasonal Physical–BioGeoChemical dynamics in Southern Ocean Marginal Ice Zone

Raghav Pathak [a], Seyed Morteza Seyedpour [a,b,*], Bernd Kutschan [c], Silke Thoms [c], Tim Ricken [a,b,*]

[a] Institute of Structural Mechanics and Dynamics in Aerospace Engineering, University of Stuttgart, Pfaffenwaldring 27, Stuttgart, 70569, Germany
[b] Porous Media Lab, Institute of Structural Mechanics and Dynamics in Aerospace Engineering, Faculty of Aerospace Engineering and Geodesy, University of Stuttgart, Pfaffenwaldring 27, Stuttgart, 70569, Germany
[c] Ecological Chemistry, Alfred Wegener Institute, Am Handelshafen 12, Bremerhaven, 27570, Germany

ARTICLE INFO

Keywords:
Antarctic sea ice
Multiscale phase transition
Multifield problems
Extended Theory of Porous Media (eTPM)
Diatom carbon assimilation
Physical–BioGeoChemical (P-BGC) processes

ABSTRACT

Sea ice in the polar oceans plays a significant role in regulating global climate and biological ecosystems. During the winter months, seawater freezes to form porous ice, which also serves as a habitat for sea ice algae to survive in harsh winter conditions. However, accurate description of mechanisms and interactions associated with formation of ice, and its interaction with photosynthesis and carbon assimilation have not been well understood. This paper presents a modeling framework to describe coupled small scale Physical (P) and BioGeoChemical (BGC) processes associated with sea ice. Critical processes associated with photosynthesis along with growth and loss of algal carbon are considered. Appropriate parametrization for environmental factors such as temperature, light, salinity, and nutrients are employed to model the photosynthetic rate. Summer and winter environmental conditions are presented and discussed in detail. Finally, monthly data is taken from literature to simulate a typical year in the Southern Ocean.

Software availability

Mathematical modeling and Analysis in this study was completed using FEAP 8.4 (http://projects.ce.berkeley.edu/feap/) developed by Prof. R.L. Taylor and colleagues. FEAP is a licensed software and therefore, sharing the source code is not possible. However, an executable version with input and procedure files can be found on the project's GitHub repository (https://github.com/Raghav2197/Multi-X_Sea_Ice_modeling). For more information on the source code, the reader is encouraged to contact the authors.

1. Introduction

The Southern Ocean in general and sea ice in particular have been acknowledged as significant components in global climate dynamics (McElroy, 1983; Martinson, 2018). The key distinction of Southern Ocean system with its Northern counterpart lies in the interaction with the Antarctic Circumpolar Current (ACC) acting as a water mass facilitating exchange of heat, gases, nutrients and carbon dioxide (CO_2) in the ocean system (Sabine et al., 2004). Along with winds averaging 15–24 knots (8–12 ms^{-1}), the ACC enhances CO_2 transfer from the atmosphere to surface water and the deeper parts of the ocean below. The Southern Ocean, thus, accounts for over 40% anthropogenically derived CO_2 coming into the global water masses, making itself the largest CO_2 sink on earth (Sabine et al., 2004; Landschützer et al., 2016; Pardo et al., 2017).

The process of transferring CO_2 from the surface to the deep ocean is mainly influenced by two mechanisms, namely the Biological Carbon Pump (BCP) and the Solubility Carbon Pump (SCP) (Volk and Hoffert, 2013). The SCP is driven by the mechanism that CO_2 is more soluble in cold water tending to sink below towards the ocean bed, taking dissolved CO_2 with it. On the contrary, the BCP is driven by either soft tissue pump or carbonate pump.

Small single celled algal species, ranging from 2 μm to 2 mm (Falkowski and Knoll, 2007), act as primary producers, synthesizing organic matter from CO_2 (Fischer et al., 2016). These tiny organisms have been studied in various environmental systems, and extensively modeled, such as soil, rivers and lakes (Bryceson et al., 2022; Pyo et al., 2019; Manteaux et al., 2023; Malve et al., 2007). However, in sea ice systems, the conditions are different. Due to freezing of

* Corresponding authors at: Institute of Structural Mechanics and Dynamics in Aerospace Engineering, University of Stuttgart, Pfaffenwaldring 27, Stuttgart, 70569, Germany.
E-mail addresses: seyed-morteza.seyedpour@isd.uni-stuttgart.de (S.M. Seyedpour), tim.ricken@isd.uni-stuttgart.de (T. Ricken).

https://doi.org/10.1016/j.envsoft.2024.106270
Received 9 August 2024; Received in revised form 2 October 2024; Accepted 13 November 2024
Available online 17 December 2024
1364-8152/

seawater and sea ice formation, these tiny microbes either passively or actively find themselves trapped in interstitial brine pockets within the ice. Thus, this non-turbulent and rather stable habitat supports algal growth on the upper ocean levels during winter (Arrigo and Van Dijken, 2003). Microbial communities have developed strategies to 'anchor' themselves to the ice matrix by producing Exopolymeric substances helping them stick to ice crystals (Krembs et al., 2002). Sea ice algae are key contributors to the seasonal dynamics of the overall primary production in the ocean waters (Thomas and Dieckmann, 2002; Arrigo and Thomas, 2004), which is specially enhanced in the Marginal Ice Zone (MIZ) (Arrigo et al., 2009). Furthermore, sea ice algae become a food source for other organisms, such as Antarctic Krill (Kohlbach et al., 2017), hence, they further extend the circulation of organic matter in the ocean system (Thomas and Dieckmann, 2010).

Sea ice in the MIZ provides a habitat or platform for the algae to grow under the ice floes and in the porous sea ice microstructures. Unlike ice masses that are associated with large temporal and spatial scales like permafrost (Zhao et al., 2022), MIZ has so far been poorly modeled and understood through simulations. Sea ice keeps them away from the cold winter atmospheric currents, while still having ample amount of sunlight to facilitate photosynthesis and net growth (Arrigo, 2017). The algal species in the sea ice zone, however, also interact strongly with salinity and nutrient availability for their growth (Zhang, 1999). The presence and growth of algae leads to strong discoloration of sea ice (Koh et al., 2012).

To understand the BioGeoChemistry of sea ice and the primary production associated with it, mathematical modeling of sea ice physical, thermodynamic, and BGC mechanisms enjoy significant importance. These mechanisms are phase transition between seawater and ice in winter, formation of microscopic brine pores and understanding of variation of environmental factors due to formation of sea ice. Considering the real pore geometry and heterogeneous microstructure of sea ice, it is computationally expensive to simulate the coupled processes in a continuum mechanical framework.

Homogenization of the microstructure is often found suitable to model highly complex and varying, heterogeneous porous materials like the sea ice. Multiphasic continuum mechanical approaches have been appropriately employed at several instances to model such material behavior. The conservation laws of mass, momentum, and energy are included, and the models are typically derived by applying the Mixture theory (MT) (Bowen, 1969; Passman, 1977; Drumheller, 1978), the Theory of Porous Media (TPM) (de Boer, 1996; Ehlers, 2002; Ehlers and Bluhm, 2011), and local volume averaging theory (Hassanizadeh and Gray, 1979a,b; Lewis and Schrefler, 1999). The primary distinctions among these models reside in the underlying motivation of the theory and the incorporation of homogenized quantities.

TPM provides a framework to describe multiphasic, multicomponent behavior of porous materials like sea ice. TPM has also been found to be suitable for modeling phase transition phenomena in porous media, cf. de Boer and Bluhm (1999) and Ricken and Bluhm (2010b). Recently, Ricken et al. (2014, 2020) introduced the extended Theory of Porous Media (eTPM) which allows for a further description of miscible solute components in the immiscible phases. TPM has also been proven as a suitable tool for modeling freezing processes (Bluhm et al., 2009; Ricken and Bluhm, 2010a; Bluhm et al., 2014; Thom and Ricken, 2021, 2019; Schwarz et al., 2020, 2021). The phase field approach is useful in modeling pattern formation and can also be utilized to determine the size of the brine channels and pores in sea ice. Thoms et al. (2014) presented an original coupled order parameter-salinity based phase field solidification model to describe brine channel formation in sea ice. Moj et al. (2017) presented an approach to model micro-macro phase transitions in the context of steel solidification using phase field on the microscale and TPM on the macroscale.

This paper presents a modeling approach to describe primary production in the sea ice zone. The BGC process of carbon assimilation is described considering all necessary environmental influences like temperature, salinity and sunlight, which are often interacting with the ice physics. TPM has been employed to model the necessary physical quantities on the macroscale. The outline of the paper is as follows. First, a multiphasic, multicomponent TPM model is set up to describe ice physics and seasonal variations in ice cover. Next, the BGC model of primary production is set up using a coupled system of Ordinary Differential Equations (ODEs) following the BioGeoChemical Flux model for sea ice (BFM-SI) (Tedesco and Vichi, 2010; Tedesco et al., 2010, 2012) and Regulated Ecosystem Model (REcoM) (Schourup-Kristensen et al., 2014; Gürses et al., 2023) and a one way coupling is created with physical variables, temperature and brine salinity, that are calculated from the TPM model. Finally, academic results are presented and discussed in detail to show a proof of concept and validity of the modeling approach, followed by concluding remarks and future directions.

2. Material and methods

2.1. Extended Theory of Porous Media (eTPM)

The fundamentals of the TPM are developed from the combination of two basic concepts, namely the theory of mixtures and the concept of volume fractions, which enable the consideration of the local composition of the overall aggregate. The extended Theory of Porous Media (eTPM) (Ricken et al., 2014; Seyedpour et al., 2022, 2023a,b) presents a method for addressing miscible substances φ^{β} present within immiscible macro phases φ^{α}. The aggregate mixture body φ consists of κ macroscopic phases denoted as φ^{α}, with $\alpha = 1, \dots, \kappa$. Furthermore, each immiscible phase can be comprised by ν components $\varphi^{\alpha\beta}$ which are resolved and transported in phase φ^{α}. The overall aggregate can be homogenized as

$$\varphi = \bigcup_{\alpha}^{\kappa} \varphi^{\alpha} := \bigcup_{\alpha}^{\kappa} \left(\bigcup_{\beta}^{\nu} \varphi^{\alpha\beta} \right). \tag{1}$$

Sea ice can be represented by the biphasic ice-seawater aggregate with $\alpha = \mathbf{I}, \mathbf{L}$. $\varphi^{\mathbf{I}}$ and $\varphi^{\mathbf{L}}$ denote the solid ice matrix and the liquid brine, respectively. The brine phase is composed of miscible components $\varphi^{\mathbf{L},\beta}$ with $\{\beta = \mathrm{s}, \mathrm{w}\}$, designated as salt (s) and freshwater (w), respectively. Through an averaging process, all phases are smeared evenly throughout the entire domain. Fig. 1 shows the decomposition from the true structure of a heterogeneous mixture body to immiscible phase of ice and liquid, followed by further decomposition to miscible liquid constituents of salt and nutrients to finally achieving a smeared body which is homogenized over the domain.

The volume fraction describes the ratio between the partial volume dv^{α} of a constituent φ^{α} and the entire volume dv as

$$\mathrm{n}^{\alpha} = \frac{\mathrm{dv}^{\alpha}}{\mathrm{dv}}. \tag{2}$$

Regarding the constraint that no vacant space within the control volume is allowed, and with the result that the sea ice is entirely saturated by the liquid brine, the saturation condition can be written as

$$\sum_{\alpha} \mathrm{n}^{\alpha} = \mathrm{n}^{\mathbf{I}} + \mathrm{n}^{\mathbf{L}} = 1. \tag{3}$$

Based on the mass of a constituent m^{α}, real density $\rho^{\alpha\mathrm{R}}$ and partial density ρ^{α} are defined by

$$\rho^{\alpha\mathrm{R}} = \frac{\mathrm{dm}^{\alpha}}{\mathrm{dv}^{\alpha}} \quad \text{and} \quad \rho^{\alpha} = \frac{\mathrm{dm}^{\alpha}}{\mathrm{dv}}. \tag{4}$$

The relation between partial and real densities can be expressed with respect to the volume fraction

$$\rho^{\alpha} = \mathrm{n}^{\alpha}\, \rho^{\alpha\mathrm{R}}. \tag{5}$$

$\rho^{\alpha\mathrm{R}}$ can also be written as a sum of real densities of the miscible components $\varphi^{\alpha\beta}$ as $\rho^{\alpha\mathrm{R}} = \sum_{\beta} \rho^{\alpha\beta}$ and, hence, the partial pore densities can be written as $\rho^{\beta} = \frac{\mathrm{dm}^{\beta}}{\mathrm{dv}} = \frac{\mathrm{dv}^{\alpha}}{\mathrm{dv}} \frac{\mathrm{dm}^{\beta}}{\mathrm{dv}^{\alpha}} = \mathrm{n}^{\alpha} \rho^{\alpha\beta}$. Considering that the

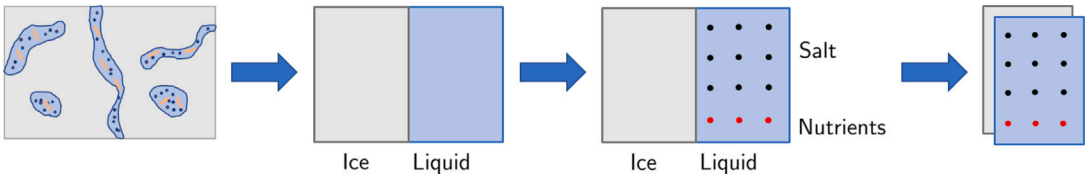

Fig. 1. Homogenization from true to smeared structure with phases.

brine liquid, which consists of the miscible components, namely fresh water and salt, brine partial density can be defined as

$$\rho^{\beta} = \frac{\mathrm{dm}^{\beta}}{\mathrm{dv}} = \frac{\mathrm{dv}^{\mathbf{L}}}{\mathrm{dv}} \frac{\mathrm{dm}^{\beta}}{\mathrm{dv}} = \mathrm{n}^{\mathbf{L}} \rho^{\mathbf{L}\beta}, \quad \text{with} \quad \rho^{\mathbf{LR}} = \sum_{\beta} \rho^{\mathbf{L}\beta} \tag{6}$$

Furthermore, the mass fraction is defined as the ratio of the solute's local mass to the total local masses of all solutes presented as $\mathrm{w}^{\mathbf{L}\beta} = \frac{\mathrm{dm}^{\beta}}{\sum_{\beta} \mathrm{dm}^{\beta}} = \frac{\rho^{\mathbf{L}\beta}}{\rho^{\mathbf{LR}}}$.

2.1.1. Kinematics

Each material point $\mathcal{P}$ of a body $\mathcal{B}$ is associated with its spatial position $\mathbf{x}$. The set containing all material points is named as the current configuration and designated with Ω_{t}, while its undeformed state is the reference configuration Ω_0.

Due to homogenization, each position $\mathbf{x}$ is associated with two material points $\mathcal{P}^{\mathbf{I}}$ and $\mathcal{P}^{\mathbf{L}}$, with individual motion functions

$$\chi_{\alpha}(\mathbf{X}, \mathrm{t}) : \left\{ \Omega_0 \to \Omega_{\mathrm{t}} : \mathbf{X}\left(\mathcal{P}^{\alpha}\right) \mapsto \mathbf{x}\left(\mathcal{P}^{\alpha}, \mathrm{t}\right), \right. \tag{7}$$

This kinematic relation is shown in Fig. 2. Derivation in time leads to the velocity of each constituent and can be written as

$$\mathbf{x}'_{\alpha} = \frac{\partial \chi_{\alpha}\left(\mathcal{P}^{\alpha}, \mathrm{t}\right)}{\partial \mathrm{t}}, \tag{8}$$

while the motion of the entire mixture is described by the barycentric velocity

$$\dot{\mathbf{x}} = \frac{1}{\rho} \sum_{\alpha} \rho^{\alpha} \mathbf{x}'_{\alpha}, \tag{9}$$

with ρ being the sum of densities of individual phases, given as $\rho = \sum \rho^{\alpha}$. Hence, the mass average velocity of the liquid brine $\mathbf{x}'_{\mathbf{L}}$ is defined as

$$\mathbf{x}'_{\mathbf{L}} = \frac{1}{\rho^{\mathbf{LR}}} \sum_{\beta} \rho^{\mathbf{L}\beta} \mathbf{x}'_{\mathbf{L}\beta} = \sum_{\beta} \mathrm{w}^{\mathbf{L}\beta} \mathbf{x}'_{\mathbf{L}\beta}. \tag{10}$$

The seepage velocity is defined to characterize the advection of brine liquid through the ice matrix and can be written as

$$\mathbf{w}_{\mathbf{LI}} = \mathbf{x}'_{\mathbf{L}} - \mathbf{x}'_{\mathbf{I}}. \tag{11}$$

Similarly, the velocity difference between the miscible components and the solid matrix is given as

$$\mathbf{w}_{\beta\mathbf{I}} = \mathbf{x}'_{\beta} - \mathbf{x}'_{\mathbf{I}}. \tag{12}$$

The diffusion velocity of the component w.r.t the moving solution can then be defined as

$$\mathbf{d}_{\beta\mathbf{L}} = \mathbf{w}_{\beta\mathbf{I}} - \mathbf{w}_{\mathbf{LI}}. \tag{13}$$

2.2. Biphasic model of sea ice with salt concentration

For the discussion of balance relations for multiphasic materials, Truesdell's "metaphysical principles" (Truesdell, 1984) of mixture theories serve as the foundation. These principles are based on the notion that the equilibrium conditions of the constituents φ^{α} and the overall mixture body φ can be represented similar to the equilibrium conditions observed in classical continuum mechanics for single-phase materials. To further describe the interaction mechanisms between the constituents, the so-called production terms are applied. The balance equations in the eTPM framework can be set up for each macroscopic phase φ^{α} and for the miscible component φ^{β}. The partial balance equations of mass, momentum, moment of momentum, and energy can be written as

$$\begin{aligned}
&\left(\rho^{\alpha}\right)'_{\alpha} + \rho^{\alpha} \operatorname{div} \mathbf{x}'_{\alpha} = \hat{\rho}^{\alpha}, \quad \left(\rho^{\beta}\right)'_{\beta} + \rho^{\beta} \operatorname{div} \mathbf{x}'_{\beta} = \hat{\rho}^{\beta} \\
&\operatorname{div} \mathbf{T}^{\alpha} + \rho^{\alpha}\left(\mathbf{b} - \mathbf{x}''_{\alpha}\right) = \hat{\rho}^{\alpha} \mathbf{x}'_{\alpha} - \hat{\mathbf{p}}^{\alpha}, \quad \operatorname{div} \mathbf{T}^{\beta} + \rho^{\beta}\left(\mathbf{b} - \mathbf{x}''_{\beta}\right) = \hat{\rho}^{\beta} \mathbf{x}'_{\beta} - \hat{\mathbf{p}}^{\beta}, \\
&\mathbf{T}^{\alpha} = \left(\mathbf{T}^{\alpha}\right)^{\mathrm{T}}, \\
&\hat{\rho}^{\alpha}\left(\varepsilon^{\alpha}\right)'_{\alpha} - \mathbf{T}^{\alpha} \cdot \mathbf{D}_{\alpha} - \rho^{\alpha} \mathrm{r}^{\alpha} + \operatorname{div} \mathbf{q}^{\alpha} = \hat{\mathrm{e}}^{\alpha} - \hat{\mathbf{p}}^{\alpha} \cdot \mathbf{x}'_{\alpha} - \hat{\rho}^{\alpha}\left(\varepsilon^{\alpha} - \frac{1}{2}\mathbf{x}'_{\alpha} \cdot \mathbf{x}'_{\alpha}\right), \\
&\hat{\rho}^{\beta}\left(\varepsilon^{\beta}\right)'_{\beta} - \mathbf{T}^{\beta} \cdot \mathbf{D}_{\beta} - \rho^{\beta} \mathrm{r}^{\beta} + \operatorname{div} \mathbf{q}^{\beta} = \hat{\mathrm{e}}^{\beta} - \hat{\mathbf{p}}^{\beta} \cdot \mathbf{x}'_{\beta} - \hat{\rho}^{\beta}\left(\varepsilon^{\beta} - \frac{1}{2}\mathbf{x}'_{\beta} \cdot \mathbf{x}'_{\beta}\right).
\end{aligned} \tag{14}$$

Here, "div(·)" is the divergence operator, $\mathbf{b}^{\alpha}$ is the mass specific body force, which is usually identified with the overall gravitational force $\mathbf{g}$, $\hat{\mathbf{p}}^{\alpha}$ is the term associated with the production of linear momentum, $\mathbf{T}^{\alpha}$ denotes partial Cauchy stress tensor of the phase φ^{α}, and $\mathbf{D}_{\alpha}$ is the symmetric part of the spatial velocity gradient $\mathbf{L} = \left(\mathbf{F}_{\alpha}\right)'_{\alpha} \mathbf{F}_{\alpha}^{-1}$ with the deformation gradient $\mathbf{F}_{\alpha}$. In the energy balance, $\varepsilon^{\alpha}, r^{\alpha}$ and $\mathbf{q}^{\alpha}$ are the internal energy, external heat supply and the heat flux, respectively.

The local supply terms for energy, momentum, and mass are denoted as $\hat{\mathrm{e}}^{\alpha}$, $\hat{\mathbf{p}}^{\alpha}$, and $\hat{\rho}^{\alpha}$, respectively. The supply terms for miscible constituents are defined in the same manner. The sum of the local balance equations across all phases must align with the balance equations for both the individual components and the entire system. Consequently, the total of the supply terms must equal zero to ensure consistency with the conservation principles (Truesdell, 1984)

$$\sum_{\alpha} \hat{\rho}^{\alpha} = 0, \quad \sum_{\alpha} \hat{\mathbf{p}}^{\alpha} = \mathbf{0}, \quad \sum_{\alpha} \hat{\mathrm{e}}^{\alpha} = 0. \tag{15}$$

2.2.1. Assumptions and field equations

In this section, the necessary assumptions and field equations for setting up the biphasic system are laid down. Assuming isothermal conditions between the phases of sea ice as a mixture ($\theta = \theta^{\alpha}$), the energy supply between the phases has to be equal to zero ($\hat{\mathrm{e}}^{\alpha} = 0$). The solid ice matrix is assumed to be incompressible ($(\rho^{\mathbf{IR}})'_{\mathbf{I}} = 0$). A density change can only arise due to variation of temperature, yielding the real density as a function of temperature ($\rho^{\mathbf{IR}} = \rho^{\mathbf{IR}}(\theta)$). The brine liquid is also incompressible, but its real density can change due to variations in salinity ($\rho^{\mathbf{LR}} = \rho^{\mathbf{LR}}\left(\mathrm{S}^{\mathrm{br}}\right)$). Hence, the mass balance for ice and brine liquid can be written

$$\begin{aligned}
&\left(\mathrm{n}^{\mathbf{I}}\right)'_{\mathbf{I}} \rho^{\mathbf{IR}} + \mathrm{n}^{\mathbf{I}} \left(\rho^{\mathbf{IR}}\right)'_{\mathbf{I}} \operatorname{div} \mathbf{x}'_{\mathbf{I}} = \hat{\rho}^{\mathbf{I}}, \\
&\left(\mathrm{n}^{\mathbf{L}}\right)'_{\mathbf{L}} \rho^{\mathbf{LR}} + \mathrm{n}^{\mathbf{L}} \left(\rho^{\mathbf{LR}}\right)'_{\mathbf{L}} \operatorname{div} \mathbf{x}'_{\mathbf{L}} = -\hat{\rho}^{\mathbf{I}}.
\end{aligned} \tag{16}$$

Within the TPM framework, it is common for the problems to arise from isothermal and quasi-static scenarios described w.r.t. the solid matrix motion. To satisfy this requirement, the fluid motion's material time derivative $(\cdot)'_{\mathbf{L}}$ must be connected to the matrix time derivative $(\cdot)'_{\mathbf{I}}$ by modifying the convective component. Given an arbitrary field function Γ, this transformation results in

$$(\Gamma)'_{\mathbf{L}} = (\Gamma)'_{\mathbf{I}} + \operatorname{grad} \Gamma \cdot \mathbf{w}_{\mathbf{LI}}. \tag{17}$$

Using Eq. (17), the mass conservation of salt can be read as

$$\mathrm{n}^{\mathbf{L}} \left(\rho^{\mathbf{L}\beta}\right)'_{\mathbf{I}} + \left(\mathrm{n}^{\mathbf{L}}\right)'_{\mathbf{I}} \rho^{\mathbf{L}\beta} \operatorname{div}^{\mathbf{L}} \rho^{\mathbf{L}\beta} \mathbf{w}_{\beta\mathbf{I}} + \mathrm{n}^{\mathbf{L}} \rho^{\mathbf{L}\beta} \operatorname{div} \mathbf{x}'_{\mathbf{I}} = 0. \tag{18}$$

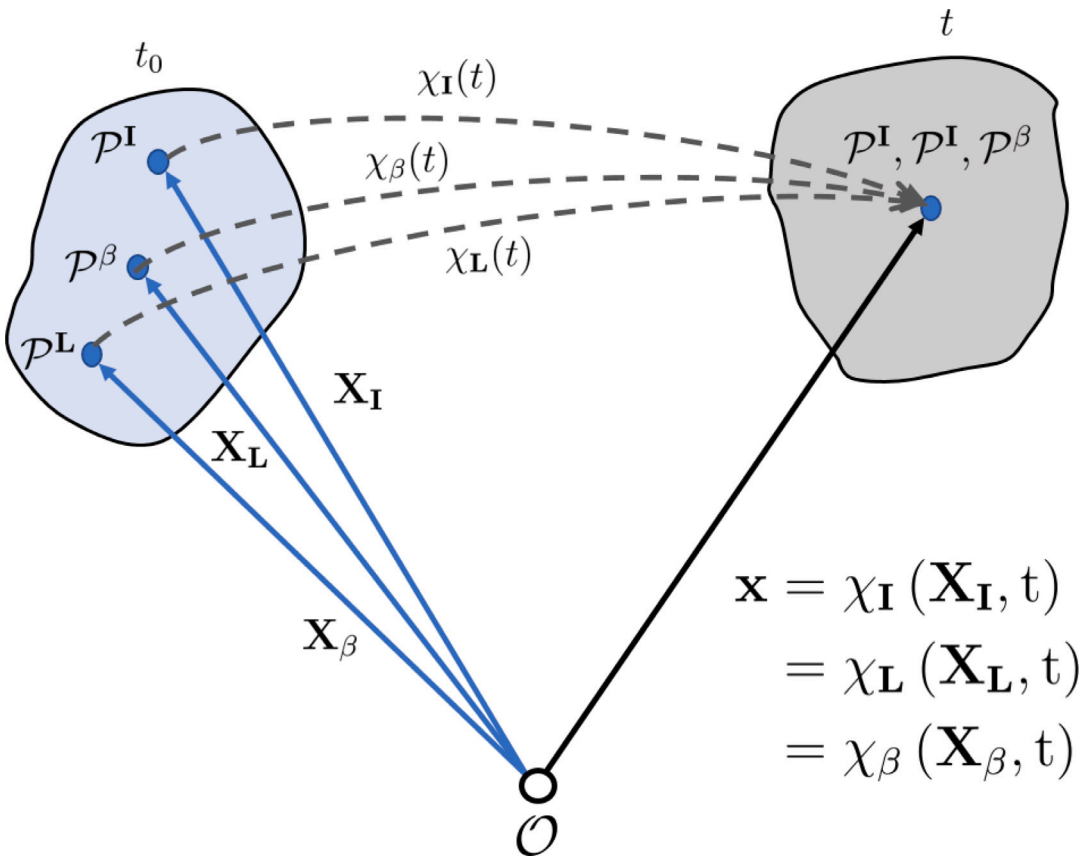

Fig. 2. Kinematics in the framework of TPM.

Proceeding from initial boundary-value problems under quasi-static conditions given by $\mathbf{x}''_{\alpha} \equiv \mathbf{0}$ given in Eq. (14)$_2$, the balance of momentum is given as

$$\operatorname{div} \mathbf{T}^{\mathbf{I}} + \rho^{\mathbf{I}} \mathrm{b} = \hat{\rho}^{\mathbf{I}} \mathbf{x}'_{\mathbf{I}} - \hat{\mathbf{p}}^{\mathbf{I}} \quad ; \quad \operatorname{div} \mathbf{T}^{\mathbf{L}} + \rho^{\mathbf{L}} \mathbf{b} = -\hat{\rho}^{\mathbf{I}} \mathbf{x}'_{\mathbf{L}} + \hat{\mathbf{p}}^{\mathbf{I}}. \tag{19}$$

Considering that the total production of linear momentum has to vanish, $\sum_{\alpha} \hat{\mathbf{p}}^{\alpha} = \mathbf{0}$, in combination with Eq. (11), the balance of linear momentum of mixture can be read as

$$\operatorname{div} \mathbf{T} + \rho \mathbf{b} = -\hat{\rho}^{\mathbf{I}} \mathbf{w}_{\mathbf{LI}}, \tag{20}$$

with $\mathbf{T} = \mathbf{T}^{\mathbf{I}} + \mathbf{T}^{\mathbf{L}}$ and $\rho = \rho^{\mathbf{I}} + \rho^{\mathbf{L}}$.

Using the specific Helmholtz free energy $\psi^{\alpha} = \varepsilon^{\alpha} - \theta^{\alpha} \eta^{\alpha}$, the energy balance for the mixture can be written as

$$\begin{aligned} &\sum_{\alpha} \left\{ \rho^{\alpha} \left[\left(\psi^{\alpha}\right)'_{\alpha} + \ (\theta)'_{\alpha} \eta^{\alpha} + \theta \left(\eta^{\alpha}\right)'_{\alpha} \right] - \mathbf{T}^{\alpha} \cdot \mathbf{D}_{\alpha} \right\} + \operatorname{div} \mathbf{q} = \\ &- \hat{\mathbf{p}}^{\mathbf{L}} \cdot \mathbf{w}_{\mathbf{LI}} - \hat{\rho}^{\mathbf{I}} \left(\psi^{\mathbf{I}} - \psi^{\mathbf{L}} + \theta \left(\eta^{\mathbf{I}} - \eta^{\mathbf{L}} \right) \right), \end{aligned} \tag{21}$$

with the total heat flux $\mathbf{q} = \mathbf{q}^{\mathbf{I}} + \mathbf{q}^{\mathbf{L}}$ and specific entropy of the phase $\eta^{\alpha} = \eta^{\alpha}(\mathbf{x}, \mathbf{t})$. The relations between brine components $\varphi^{\mathbf{L}\beta}$ and the overall mixture $\varphi^{\mathbf{L}}$ can be written as

$$\mathbf{T}^{\mathbf{L}} = \sum_{\beta} \mathbf{T}^{\mathbf{L}\beta}, \quad \eta^{\mathbf{L}} = \sum_{\beta} \eta^{\mathbf{L}\beta}, \quad \psi^{\mathbf{L}} = \sum_{\beta} \psi^{\mathbf{L}\beta} \tag{22}$$

2.2.2. Constitutive relations

In addition to the balance Eqs. (14), constitutive relations for the stresses $\mathbf{T}^{\mathbf{I}}$ and $\mathbf{T}^{\mathbf{L}}$, seepage velocity $\mathbf{w}_{\mathbf{LI}}$ and the mass exchange rate $\hat{\rho}^{\mathbf{I}}$ are required. In order to ensure thermodynamically consistent solutions, these are evaluated using the entropy inequality. In multi-phase material modeling, it is conventional to incorporate the material time derivative of the saturation condition, along with the Lagrange multiplier λ, as an additional constraint in the entropy inequality. To achieve a more practical energy formulation, the specific Helmholtz free energy, denoted as ψ^{α}, is utilized by the equation $\psi^{\alpha} = \varepsilon^{\alpha} - \theta^{\alpha} \eta^{\alpha}$. Consequently, the local version of the Clausius-Duhem entropy inequality can be read

$$\begin{aligned} &\sum_{\alpha} \left\{ -\rho^{\alpha} \left[\left(\psi^{\alpha}\right)'_{\alpha} + (\theta)'_{\alpha} \eta^{\alpha} \right] + \mathbf{T}^{\alpha} \cdot \mathbf{D}_{\alpha} - \frac{1}{\theta} \operatorname{grad} \theta \cdot \mathbf{q}^{\alpha} \right\} \\ &\left\{ -\hat{\rho}^{\alpha} \left(\psi^{\alpha} - \frac{1}{2} \mathbf{x}'_{\alpha} \cdot \mathbf{x}'_{\alpha} \right) \ - \hat{\mathbf{p}}^{\alpha} \cdot \mathbf{x}'_{\alpha} \right\} + \lambda \left\{ \left(1 - \sum_{\alpha} \mathrm{n}^{\alpha} \right)'_{\mathbf{I}} \right\} \geq 0. \end{aligned} \tag{23}$$

In order to account for the multi-component nature of the system, a mass-specific Helmholtz free energy, denoted as ψ^{β}, is introduced. By summing up this energy over all the components, we obtain the Helmholtz free energy of the liquid brine $\psi^{\mathbf{L}}$ as the sum of the components

$$\rho^{\beta} \psi^{\beta} = \mathrm{n}^{\mathbf{L}} \left(\rho^{\mathbf{L}\beta} \psi^{\beta} \right) = \mathrm{n}^{\mathbf{L}} \psi^{\mathbf{L}\beta} \quad \text{with} \quad \sum_{\beta} \psi^{\mathbf{L}\beta} = \sum_{\beta} \rho^{\mathbf{L}\beta} \psi^{\beta} = \psi^{\mathbf{L}}. \tag{24}$$

In order to keep the complexity of the evaluation in a justifiable scope, the dependency of the Helmholtz free energies $\psi^{\mathbf{I}}$ and $\psi^{\mathbf{L}\beta}$ is restricted on the following process variables as follows

$$\psi^{\mathbf{I}} = \psi^{\mathbf{I}} \left(\mathbf{C}_{\mathbf{I}}, \theta \right), \quad \psi^{\mathbf{L}\beta} = \psi^{\mathbf{L}\beta} \left(\rho^{\mathbf{L}\beta}, \theta \right), \tag{25}$$

and the material time derivatives of mass specific Helmholtz energy can be read as

$$\begin{aligned} \rho^{\mathbf{I}} \left(\psi^{\mathbf{I}}\right)'_{\mathbf{I}} &= 2 \rho^{\mathbf{I}} \mathbf{F}_{\mathbf{I}} \frac{\partial \psi^{\mathbf{I}}}{\partial \mathbf{C}_{\mathbf{I}}} \left(\mathbf{F}_{\mathbf{I}}\right)^{\mathrm{T}} \cdot \mathbf{D}_{\mathbf{I}} + \rho^{\mathbf{I}} \frac{\partial \psi^{\mathbf{I}}}{\partial \theta} (\theta)'_{\mathbf{I}}, \\ \left(\psi^{\mathbf{L}\beta}\right)'_{\beta} &= \frac{\partial \psi^{\mathbf{L}\beta}}{\partial \rho^{\mathbf{L}\beta}} \left(\rho^{\mathbf{L}\beta}\right)'_{\beta} + \frac{\partial \psi^{\mathbf{L}\beta}}{\partial \rho^{\mathbf{L}\beta}} (\theta)'_{\beta}, \\ \rho^{\beta} \left(\psi^{\beta}\right)'_{\beta} &= \rho^{\beta} \left(\frac{\partial \psi^{\mathbf{L}\beta}}{\partial \rho^{\mathbf{L}\beta}} \right) = \frac{\rho^{\beta}}{\rho^{\mathbf{L}\beta}} \left(\psi^{\mathbf{L}\beta}\right)'_{\beta} - \frac{\rho^{\beta}}{\left(\rho^{\mathbf{L}\beta}\right)^2} \psi^{\mathbf{L}\beta} \left(\rho^{\mathbf{L}\beta}\right)'_{\beta}. \end{aligned} \tag{26}$$

After adding the material time derivative of saturation condition multiplied with Lagrange multiplier, and some rearrangement, the entropy inequality can be written as

$$\begin{aligned}
&\mathbf{D_I}\cdot\left\{\mathbf{T^I}+\frac{\mathrm{n^I}}{\rho^{\mathbf{IR}}}\left(\rho^{\mathbf{IR}}\right)'_{\mathbf{I}}\lambda\mathbf{I}-2\rho^{\mathbf{I}}\mathbf{F_I}\frac{\partial\psi^{\mathbf{I}}}{\partial\mathbf{C_I}}\left(\mathbf{F_I}\right)^{\mathrm{T}}\right\}-(\theta)'_{\mathbf{I}}\left\{\rho^{\mathbf{I}}\eta^{\mathbf{I}}+\rho^{\mathbf{I}}\frac{\partial\psi^{\mathbf{I}}}{\partial\theta}\right\}\\
&+\sum_{\beta}\mathbf{D}_{\beta}\cdot\left\{\mathbf{T}^{\beta}+\mathrm{n^L w^{L\beta}}\lambda\mathbf{I}\right\}-(\theta)'_{\beta}\left\{\rho^{\beta}\eta^{\beta}+\rho^{\beta}\frac{\partial\psi^{\mathbf{L}\beta}}{\partial\theta}\right\}\\
&-\sum_{\beta}\left(\rho^{\mathbf{L}\beta}\right)'_{\beta}\left\{\frac{\rho^{\beta}}{\rho^{\mathbf{L}\beta}}\frac{\partial\psi^{\mathbf{L}\beta}}{\partial\rho^{\mathbf{L}\beta}}+\lambda\frac{\mathrm{n^L}}{\rho^{\mathbf{LR}}}-\frac{\rho^{\beta}}{\left(\rho^{\mathbf{L}\beta}\right)^2}\psi^{\mathbf{L}\beta}\right\}\\
&-\hat{\rho}^{\mathbf{I}}\left\{\psi^{\mathbf{I}}-\psi^{\mathbf{L}}+\lambda\left(\frac{1}{\rho^{\mathbf{IR}}}-\frac{1}{\rho^{\mathbf{LR}}}\right)\right\}-\sum_{\beta}\mathbf{w}_{\beta\mathbf{I}}\cdot\left\{\mathrm{w^{L\beta}}\lambda\,\mathrm{grad}^{\mathbf{L}}+\hat{\mathbf{p}}^{\beta}\right\}\\
&-\frac{1}{\theta}\,\mathrm{grad}\,\theta\cdot\mathbf{q}\geq 0.
\end{aligned}\tag{27}$$

The evaluation of the Clausius-Duhem entropy inequality yields energy-conserving and dissipative limitations that must be taken into account for selecting potential functions $\psi^{\mathbf{I}}$, $\psi^{\mathbf{L}}$, and ψ^{β}. The energy conserving and dissipative parts can be defined as

$$\begin{aligned}
&\mathbf{T^I}=-\mathrm{n^I}\lambda\left(\frac{\left(\rho^{\mathbf{IR}}\right)'_{\mathbf{I}}}{\rho^{\mathbf{IR}}}\right)\mathbf{I}+\mathbf{T}^{\mathbf{I}}_{\mathrm{E}},\quad\sum_{\beta}\mathbf{T}^{\beta}=\mathbf{T^L}=-\mathrm{n^L}\lambda\mathbf{I},\\
&\text{with}\quad\mathbf{T}^{\mathbf{I}}_{\mathrm{E}}=2\rho^{\mathbf{I}}\mathbf{F_I}\frac{\partial\psi^{\mathbf{I}}}{\partial\mathbf{C_I}}\mathbf{F}^{\mathrm{T}}_{\mathbf{I}},\\
&\lambda=-\rho^{\mathbf{LR}}\left(\sum_{\beta}\frac{\partial\psi^{\mathbf{L}\beta}}{\partial\rho^{\mathbf{L}\beta}}+\frac{1}{\rho^{\mathbf{L}\beta}}\psi^{\mathbf{L}\beta}\right),\\
&\eta^{\mathbf{I}}=-\frac{\partial\psi^{\mathbf{I}}}{\partial\theta},\quad\eta^{\beta}=-\frac{1}{\rho^{\mathbf{L}\beta}}\frac{\partial\psi^{\mathbf{L}\beta}}{\partial\theta},
\end{aligned}\tag{28}$$

and

$$\begin{aligned}
&\hat{\rho}^{\mathbf{I}}=-\delta_{\mu\mathbf{I}}\left(\mu^{\mathbf{I}}-\mu^{\mathbf{L}}\right),\\
&\text{with}\;\mu^{\mathbf{I}}=\psi^{\mathbf{I}}+\frac{\lambda}{\rho^{\mathbf{IR}}},\quad\mu^{\mathbf{L}}=\psi^{\mathbf{L}}+\frac{\lambda}{\rho^{\mathbf{LR}}},\\
&\hat{\mathbf{p}}^{\beta}=\mathrm{w^{L\beta}}\lambda\,\mathrm{grad}\mathrm{n}^{\mathbf{L}}+\hat{\mathbf{p}}^{\beta}_{\mathrm{E}},\quad\hat{\mathbf{p}}^{\beta}_{\mathrm{E}}=-\delta_{\mathbf{w}_{\beta\mathbf{I}}}\mathbf{w}_{\beta\mathbf{I}},\\
&\mathbf{q}=-\alpha_{\nabla\theta}\,\mathrm{grad}\,\theta.
\end{aligned}\tag{29}$$

Based on the principles of Rational Thermodynamics, the biphasic model for sea ice can be analyzed to determine the Cauchy stress relations. Eq. (28) provides the Cauchy stress relations for the solid ice $\mathbf{T^I}$ and brine liquid $\mathbf{T^L}$. The split for $\mathbf{T^I}$ follows from the concept of effective stresses. This analysis reveals that the solid and fluid stresses, as well as the linear momentum productions, can be divided into two terms. The first term is influenced by the pore-pressure variables, while the second term, known as the "extra term", is a result of either the solid deformation (effective stress) or the pore-fluid flow (frictional stress). The pore pressure part is also dependent on the density change $\left(\rho^{\mathbf{IR}}\right)'_{\mathbf{I}}$. λ in Eq. (28) can be identified as a pore pressure $\mathrm{p^{LR}}$. The pressure constraint incorporates the chemical potential definition $\mu^{\mathbf{L}\beta}=\partial\psi^{\mathbf{L}\beta}/\partial\rho^{\mathbf{L}\beta}$. In addition to pressure changes caused by hydraulic impacts, the model can also incorporate changes resulting from variations in chemical composition due to diffusion, osmosis, or reaction by utilizing the chemical potential. The relation for the specific entropies in Eq. (28) is obtained by deriving the specific Helmholtz free energy with respect to the temperature.

By implementing the restriction for momentum exchange $(29)_3$ into the momentum balance for component φ^{β}, a constitutive relation for the mass flux with respect to the solid ice can be derived, which consists of an advective $\left(\mathbf{w_{LI}}\right)$ and diffusive $\left(\mathbf{w}_{\beta\mathbf{L}}\right)$ part as

$$\mathbf{j}^{\beta}=\mathrm{n^L}\mathbf{j}^{\mathbf{L}\beta}=\mathrm{n^L}\rho^{\mathbf{L}\beta}\mathbf{w}_{\beta\mathbf{I}}=\mathrm{n^L}\rho^{\mathbf{L}\beta}\left(\mathbf{w_{LI}}+\mathbf{w}_{\beta\mathbf{L}}\right),\tag{30}$$

and the total mass flux formulation reads

$$\mathbf{j}^{\beta}=\mathrm{n^L}\rho^{\mathbf{L}}\mathbf{w}_{\beta\mathbf{I}}=-\mathrm{n^L w^{L\beta}}\mathrm{D}_{\mathbf{L}\beta}\,\mathrm{grad}\,\mathrm{p^{LR}}-\rho^{\mathbf{L}\beta}\frac{\mathrm{K^I}}{\eta^{\mathbf{LR}}}\,\mathrm{grad}\,p^{\mathbf{LR}},\tag{31}$$

wherein $\mathrm{D}_{\mathbf{L}\beta}$ represents the diffusion coefficient of component φ^{β} in mixture $\varphi^{\mathbf{L}}$, $\mathrm{K^I}$ is the intrinsic permeability and $\eta^{\mathbf{LR}}$ is the dynamic viscosity of the mixture. The restriction for the heat flux vector $\mathbf{q}$ gained from the dissipation mechanism can directly be identified as Fourier's law, which describes the heat conduction negative proportional to the temperature gradient with $\alpha_{\nabla\theta}$ as the heat conduction coefficient.

Brine salinity ($\mathrm{S^{br}}$) is modeled using the local salinity-temperature equilibrium as the salinity of the brine trapped within the pores and is generally defined as a third order polynomial fit to observations (Dawson et al., 2023; Thomas, 2017; Notz and Worster, 2009). The relation is given as

$$\mathrm{S^{br}}=-21.4\,\theta-0.886\,\theta^2-0.0170\,\theta^3.\tag{32}$$

The difference in specific enthalpies of liquid ($\mathrm{h^L}$) and ice ($\mathrm{h^I}$) determine the latent heat of phase change between seawater and ice. The mass production term $\hat{\rho}^{\mathbf{I}}$ affects the volume fraction of ice, the pore pressure and the temperature in the system. In the balance of energy of the mixture, Eq. (38), $\hat{\rho}^{\mathbf{I}}$ is multiplied with the difference of ($\mathrm{h^L}$) and ($\mathrm{h^I}$), hence incorporating also the latent heat of phase transition.

2.3. Numerical treatment

Once the necessary assumptions, governing equations, and constitutive relations are established, the weak formulations for the finite element simulation need to be developed in order to calculate the unknown field quantities. The remaining unknown quantities are summarized here as

$$\mathcal{R}=\mathcal{R}(\mathbf{x},\mathbf{t})=\left\{\mathbf{u_I},\,\mathbf{n^I},\,\mathrm{S^{Bulk}_{Macro}},\,\mathrm{p^{LR}},\,\theta\right\},\tag{33}$$

where $\mathbf{u_I}$, $\mathbf{n^I}$, $\mathrm{S^{Bulk}_{Macro}}$, $\mathrm{p^{LR}}$, and θ are the deformation of ice matrix, volume fraction of ice, bulk salinity on the macroscale, pore pressure that the brine liquid is exerting on the ice matrix, and the temperature of the mixture body. Standard Galerkin Finite Element Method (FEM) (Zienkiewicz et al., 2013) is used to derive the weak formulations for the unknown field quantities. The weak forms for the mass balance of ice, mass balance of mixture, concentration balance of salt, momentum balance of the mixture and energy balance for the mixture read

$$\bullet\quad\int_{\mathrm{B_I}}\left\{\left(\mathrm{n^I}\right)'_{\mathbf{I}}\rho^{\mathbf{IR}}+\mathrm{n^I}\left(\rho^{\mathrm{IR}}\right)'_{\mathbf{I}}\mathrm{tr}_{\mathbf{I}}-\hat{\rho}^{\mathbf{I}}\right\}\delta\mathrm{n^I}\mathrm{dv}=0,\tag{34}$$

$$\begin{aligned}
\bullet\quad&\int_{\mathrm{B_I}}\left\{\mathrm{n^L}\left(\mathrm{S^{br}}\right)'_{\mathbf{I}}+\left(\mathrm{n^L}\right)'_{\mathbf{I}}\mathrm{S^{br}}+\frac{\mathrm{n^L}}{\rho^{\mathbf{LR}}}\mathrm{S^{br}}\left(\rho^{\mathrm{LR}}\right)'_{\mathbf{I}}+\mathrm{n^L S^{br}}\mathrm{tr}\mathbf{D_I}\right\}\delta\mathrm{S^{bulk}_{Macro}}\mathrm{dv}\\
&-\int_{\mathrm{B_I}}\left\{\frac{\mathbf{j}^{\mathrm{Ls}}}{\rho^{\mathrm{LR}}}\cdot\mathrm{grad}\,\delta\mathrm{S^{bulk}_{Macro}}\right\}\mathrm{dv}=\int_{\partial\mathrm{B_I}}\left\{\frac{\mathbf{j}^{\mathrm{Ls}}}{\rho^{\mathrm{LR}}}\delta\mathrm{S^{bulk}_{Macro}}\cdot\mathbf{n}\right\}\mathrm{da},
\end{aligned}\tag{35}$$

$$\begin{aligned}
\bullet\quad&\int_{\mathrm{B_I}}-\left\{\mathrm{n^L}\mathbf{w_{LI}}\cdot\mathrm{grad}\,\delta\mathrm{p^{LR}}\right\}\mathrm{dv}+\int_{\mathrm{B_I}}\left\{\mathrm{tr}\,\mathbf{D_I}+\sum_{\alpha}\frac{\mathrm{n}^{\alpha}}{\rho^{\alpha\mathrm{R}}}\left(\rho^{\alpha\boldsymbol{R}}\right)'_{\mathbf{I}}\right.\\
&\left.-\hat{\rho}^{\mathbf{I}}\left(\frac{1}{\rho^{\mathrm{LR}}}-\frac{1}{\rho^{\mathrm{IR}}}\right)\right\}\delta\mathrm{p^{LR}}\mathrm{dv}=-\int_{\partial\mathrm{B_I}}\left\{\mathbf{n^L}\mathbf{w_{LI}}\delta\mathrm{p^{LR}}\cdot\mathbf{n}\right\}\mathrm{da},
\end{aligned}\tag{36}$$

$$\bullet\quad\int_{\mathrm{B_I}}\left(\sum_{\alpha}^{\mathbf{II}}\mathbf{T}^{\alpha}\right)\cdot\mathrm{grad}\,\delta\mathbf{u_I}\mathrm{dv}-\int_{\mathrm{B_I}}\left(\sum_{\alpha}^{\mathbf{II}}\rho^{\alpha}\right)\mathbf{b}\cdot\delta\mathbf{u_I}\mathrm{dv}=\int_{\partial\mathrm{B_I}}\left\{\mathbf{t}\cdot\delta\mathbf{u_I}\right\}\mathrm{da},\tag{37}$$

$$\begin{aligned}
\bullet\quad&\int_{\mathrm{B_I}}\left\{\theta\rho^{\mathbf{I}}\left(\eta^{\mathbf{I}}\right)'_{\mathbf{I}}\right\}\delta\theta\mathrm{dv}+\int_{\mathrm{B_I}}\left\{\theta\rho^{\mathbf{L}}\left(\eta^{\mathbf{L}}\right)'_{\mathbf{L}}\right\}\delta\theta\mathrm{dv}-\int_{\mathrm{B_I}}\left\{\mathbf{q}\cdot\mathrm{grad}\,\delta\theta\right\}\mathrm{dv}\\
&+\int_{\mathrm{B_I}}\left\{\hat{\mathbf{p}}^{\mathbf{I}}_{\mathrm{E}}\cdot\mathbf{w_{LI}}\right\}\delta\theta\mathrm{dv}+\int_{\mathrm{B_I}}\left\{\hat{\rho}^{\mathbf{I}}\left[\mathrm{h^L}-\mathrm{h^I}\right]\right\}\delta\theta\mathrm{dv}=\int_{\partial\mathrm{B_I}}\left\{\mathbf{q}\delta\theta\cdot\mathbf{n}\right\}\mathrm{da}.
\end{aligned}\tag{38}$$

The coupled system of equations is discretized in space using classical Taylor Hood elements, with the deformations being associated with quadratic elements and the other variables of interest are resolved with linear elements. The Newmark's scheme with the parameters $\alpha = 0.25$ and $\beta = 0.5$ is utilized for temporal discretization.

This results in a closed system of equations, providing a framework for description of the macroscopic behavior of sea ice. However, the ice formation phenomenon originates from the microscale pattern formation and phase transition between ice and brine phases and separation between regions of ice and saline pores. In order to model the coupled evolution of microscale volume fraction and salinity, a modified Landau Ginzburg energy function $\Omega_{LG} = \int \omega_{LG} dL_{micro}$ is used and reads

$$\omega_{LG} = \underbrace{\frac{1}{4}(a\mathrm{n}^{\mathbf{I}}_{\mathrm{micro}})^4 - \frac{1}{2}(a\mathrm{n}^{\mathbf{I}}_{\mathrm{micro}})^3 + \left(\frac{1}{4} - \frac{1}{2}\left(m - \frac{1}{2}\sigma\right)\right)\left(a\mathrm{n}^{\mathbf{I}}_{\mathrm{micro}}\right)^2 + \frac{\beta_1}{2}\sigma^2}_{\omega_L} + \underbrace{\frac{1}{2}L_c^2\left(\frac{\partial \mathrm{n}^{\mathbf{I}}_{\mathrm{micro}}}{\partial L_{micro}}\right)^2}_{\omega_G}. \tag{39}$$

where $\mathrm{n}^{\mathbf{I}}_{\mathrm{micro}}$ and σ are microscale volume fraction and salinity, respectively. The evolution equations for the microscale volume fraction $\mathrm{n}^{\mathbf{I}}_{\mathrm{micro}}$ and salinity σ can be derived as

$$\begin{aligned}\tau_0 \frac{\partial \mathrm{n}^{\mathrm{I}}_{\mathrm{micro}}}{\partial \tau} &= -\frac{\delta \omega_{LG}}{\delta \mathrm{n}^{\mathrm{I}}_{\mathrm{micro}}} = -\frac{\partial \omega_L}{\partial \mathrm{n}^{\mathrm{I}}_{\mathrm{micro}}} + L_c^2 \frac{\partial^2 \mathrm{n}^{\mathrm{I}}_{\mathrm{micro}}}{\partial L^2_{\mathrm{micro}}} \\ &= a^2 \mathrm{n}^{\mathrm{I}}_{\mathrm{micro}} \left(-a^2 \left(\mathrm{n}^{\mathrm{I}}_{\mathrm{micro}}\right)^2 + \frac{3}{2} a \mathrm{n}^{\mathrm{I}}_{\mathrm{micro}} - \frac{1}{2} + m - \frac{1}{2}\sigma\right) \\ &\quad + L_c^2 \frac{\partial^2 \mathrm{n}^{\mathrm{I}}_{\mathrm{micro}}}{\partial L^2_{\mathrm{micro}}},\end{aligned} \tag{40}$$

$$\begin{aligned}\tau_0 \frac{\partial \sigma}{\partial \tau} &= -\frac{\partial^2}{\partial L^2_{\mathrm{micro}}}\left(-\frac{\delta \omega_{LG}}{\delta \sigma}\right) = \frac{\partial^2}{\partial L^2_{\mathrm{micro}}} \frac{\partial \omega_{LG}}{\partial \sigma} \\ &= L_c^2 \frac{\partial^2}{\partial L^2_{\mathrm{micro}}}\left(\frac{1}{4} a^2 \left(\mathrm{n}^{\mathrm{I}}_{\mathrm{micro}}\right)^2 + \beta_1 \sigma\right).\end{aligned} \tag{41}$$

The coupled system of equations are discretized spatially using the Fourier transforms. Temporal discretization is achieved using the exponential time differencing scheme (ETD2) (Cox and Matthews, 2002). ETD2 is suitable to solve stiff differential equations of the type $\dot{y} = ry + z(y,t)$ with a linear term ry and a non-linear part $z(y,t)$ that correspond to the energy functional used for phase separation between brine and ice.

The macroscopic phase transition term is derived considering heat fluxes of ice $\mathbf{q}^{\mathbf{I}}$ and liquid $\mathbf{q}^{\mathbf{L}}$, latent heats of ice $\mathrm{h}^{\mathbf{I}}$ and liquid $\mathrm{h}^{\mathbf{L}}$ and the normal direction of gradient of temperature $\mathbf{n}_\Gamma$, and can be written as

$$\hat{\rho}^{\mathbf{I}} = a_\Gamma \frac{\left(\mathbf{q}^{\mathbf{L}} - \mathbf{q}^{\mathbf{I}}\right) \cdot \mathbf{n}_\Gamma}{\left(\mathrm{h}^{\mathbf{L}} - \mathrm{h}^{\mathbf{I}}\right)}, \tag{42}$$

where a_Γ is the microscale pore size derived as a function of microscale volume fraction given in Eq. (40) and reads

$$a_\Gamma = a_\Gamma(\mathrm{n}^{\mathbf{I}}_{\mathrm{micro}}). \tag{43}$$

a_Γ is simulated across a range of input temperatures and upscaled on the macroscale as a parametrized function of microscale volume fraction. This allows for a thermodynamically motivated phase transition ansatz (42) with the added information from microscale.

3. Primary production in sea ice

The process of photosynthesis and conversion of inorganic carbon to organic matter, also known as primary production is dependent on several environmental factors such as temperature, light, nutrients and salinity of the brine pockets, where the sea ice microbial communities exist. Light is usually sufficient for photosynthesis, except for regions of sea ice that have a thick snow cover (Grossi et al., 1987). While availability of light regulates the beginning of algal blooms, nutrient limitation sets the extent and magnitude of the blooms (Kirst and Wiencke, 1995). A coupled effect of temperature and salinity is observed on the primary production, owing to the fact that brine salinity is dependent on temperature due to the local thermal equilibrium given in Eq. (32). The overall carbon assimilation, however, is dependent on various interaction processes of the algae with its environment such as gross primary production, remineralization from ice-ocean interface, respiration loss, exudation or excretion loss, and loss due to lysis or death of algal species.

While more than 1000 species of diatoms exist in the MIZ of polar oceans, the discussion in this paper is restricted to a generic sea ice diatom species, characterized by a silica cell wall. Fig. 3 depicts all critical processes and environmental factors that are associated with the diatom along with the various nutrients that are influenced by these processes.

3.1. Photosynthesis

In this section, equations are derived for photosynthetic rate and its dependency on environmental forcing functions for temperature, salinity, light, and nutrients following the Biogeochemical Flux Model in a sea ice system (BFM-SI) presented in Tedesco et al. (2012). The functions are multiplicative and act as non-dimensional weights varying between 0 and 1 that are associated with each environmental factor, hence, determining the influence of each environmental factor on the total photosynthesis. The photosynthetic rate is given as

$$\hat{\rho}^{gpp} = \hat{\rho}^{gpp}_{\max} F_{PAR} F_N F_s F_\theta, \tag{44}$$

where $\hat{\rho}^{gpp}_{\max}, F_{PAR}, F_N, F_s$, and F_θ are the maximum possible photosynthesis rate, light, nutrient, salinity, and temperature dependence, respectively. The light availability is dependent on the part of total sunlight that is beneficial for photosynthesis, known as the Photosynthetically Active Radiation (PAR). Light dependence F_{PAR} is given as

$$F_{PAR} = 1 - e^{-\frac{E_{PAR}}{E_k}}, \tag{45}$$

where E_{PAR} is the available PAR, further parametrized along depth according to Beer–Lambert law given as

$$E_{PAR}(z) = \varepsilon_{PAR} F_{sw} e^{(\lambda_s + \lambda_i)z + \int_z^0 \lambda_{\mathrm{bio}}\ (z')dz'}, \tag{46}$$

where F_{sw} is the total incident radiation, ε_{PAR} is the coefficient determining the fraction of total incident light, which is available for photosynthesis. λ_s, λ_i, and λ_{bio} are the extinction coefficients due to snow, ice and biological communities, respectively. For the present study, it was assumed that ice starts growing from crystals during winter. Hence, there is no attenuation from snow and biological communities yet on light availability. The light saturation parameter E_k is the ratio between the maximum photosynthetic rate $\hat{\rho}^{gpp}_{\max}$ and the maximum light utilization coefficient α can be written as

$$E_K = \frac{\hat{\rho}^{gpp}_{\max}}{\alpha}. \tag{47}$$

Due to the silica-based cell wall, diatom growth is often limited by the available dissolved silicates in the sea ice matrix environment. The silica limitation is modeled as

$$F_N = \frac{I^{Si}}{I^{Si} + d_{Si}}, \tag{48}$$

where I^{Si} is the available dissolved silicate and d_{Si} is the half saturation value for Silica limitation. Standard seawater salinities are usually optimal for photosynthesis, and deviation from these lead to an inhibited growth (Arrigo and Sullivan, 1992). Other limiting nutrients can also be studied by replacing the terms in the above equation.

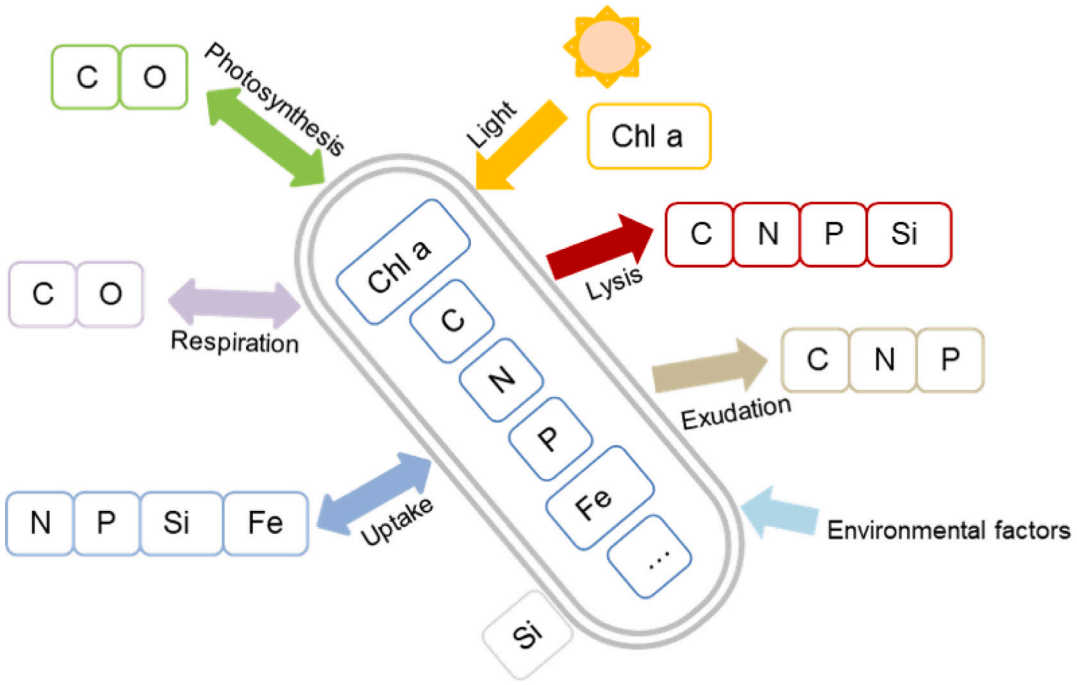

Fig. 3. Schematic diagram of a generic sea ice diatom species.

Salinity dependency is modeled using a power-log Gaussian fit given as

$$F_s = \exp\left[-\left(2.16 - 8.3\times10^{-5}.(\mathrm{S^{br}})^{2.11} - 0.55\ln(\mathrm{S^{br}})\right)^2\right], \tag{49}$$

and the temperature dependency is modeled as

$$F_\theta = (Q_{10})^{\frac{\theta-10}{10}}, \tag{50}$$

where Q_{10} is the characteristic doubling temperature parameter. The behavior of each function can be seen in Fig. 4.

3.2. Carbon assimilation

The total rate of change of carbon by diatoms is given as

$$(C_C)' = \left(\hat{\rho}^{gpp} - \hat{\lambda}^{rsp} - \hat{\lambda}^{exu} - \hat{\lambda}^{lys} + \hat{\rho}^{bdy}\right) C_C, \tag{51}$$

where $\hat{\rho}^{gpp}$, $\hat{\lambda}^{rsp}$, $\hat{\lambda}^{exu}$, $\hat{\lambda}^{lys}$, $\hat{\rho}^{bdy}$, and C_C are rate of photosynthesis, respiration, exudation, lysis, uptake from the ocean and the assimilated carbon concentration, respectively. All loss mechanisms are parametrized with respect to the photosynthesis rate. The loss due to exudation is given as

$$\hat{\lambda}^{exu} = \left[\beta + (1-\beta)\left(1 - f^{N,P}\right)\right]\hat{\rho}^{gpp}, \tag{52}$$

where β_A is a constant fraction of produced carbon that is excreted, and $f^{N,P}$ is a regulating factor for internal nutrient limitation given as

$$f^{N,P} = min\left(1, \frac{C_N/C_C - N^{min}}{N^{opt} - N^{min}}, \frac{C_P/C_C - P^{min}}{P^{opt} - P^{min}}\right), \tag{53}$$

where C_N, and C_P are internal nitrate and phosphate quotas. $(X)^{min}$, and $(X)^{opt}$ are the minimum and optimum ratios of the respective nutrient. The rate of respiration loss is then determined from the remaining carbon, considering both production and exudation loss, and is given as

$$\hat{\lambda}^{rsp} = F_\theta\, b\, C_C + \gamma\left(\hat{\rho}^{gpp} - \hat{\lambda}^{exu}\right), \tag{54}$$

where b, and γ are the specific respiration rate and constant determining respiration due to activity by algae. Finally, the loss due to lysis reads

$$\hat{\lambda}^{lys} = \frac{1}{f^{N,P} + d^{N,P}} d_0 C_C, \tag{55}$$

where $d^{N,P}$ and d_0 are the nutrient threshold and maximum possible lysis rate, respectively. The carbon assimilation by diatoms is also regulated by nutrient dynamics within the cells. Key macronutrients responsible for carbon assimilation are Phosphates, Nitrates, Ammonia, Silica and Chlorophyll-a.

The temporal evolution of concentration of internal phosphates are given as

$$(C_P)' = \hat{\rho}^{upt}_{I^{PO_4}} - \hat{\lambda}^{lys}_{PO_4}, \tag{56}$$

where $\hat{\rho}^{upt}_{I^{PO_4}}$ denotes uptake of inorganic phosphate (I^{PO_4}) from the sea ice environment and $\hat{\lambda}^{lys}_{PO_4}$ denotes the loss due to detritus. The relations for uptake and lysis read

$$\hat{\rho}^{upt}_{I^{PO_4}} = \min\left(a^{PO_4} I^{PO_4} C_C, P^{opt} G + F_\theta \hat{\rho}^{gpp}_{\max}\left(P^{max} - \frac{C_P}{C_C}\right) C_C\right), \tag{57}$$

where G is the net carbon assimilation without remineralization from ocean given as

$$G = \left(\hat{\rho}^{gpp} - \hat{\lambda}^{rsp} - \hat{\lambda}^{exu} - \hat{\lambda}^{lys}\right), \tag{58}$$

and the lysis rate of phosphate is written as

$$\hat{\lambda}^{lys}_{PO_4} = P^{min}\hat{\lambda}^{lys}. \tag{59}$$

Nitrogen comes from two sources, namely Nitrates (I^{NO_3}) and Ammonia (I^{NH_4}) and the loss is due to detritus. The concentration balance of Nitrogen and the uptake of Nitrogen is given as

$$\begin{aligned}(C_N)' &= \sum_{i=NO_3,NH_4} \hat{\rho}^{upt}_{I^i} - \hat{\lambda}^{lys}_N,\\ \sum_{i=NO_3,NH_4} \hat{\rho}^{upt}_{I^i} &= \min\left(\left(\sum_i a^i I^i\right) C_C,\right.\\ &\left. N^{opt} G + f_\theta \hat{\rho}^{gpp}_{\max}\left(N^{max} - \frac{C_N}{C_C}\right) C_C\right),\end{aligned} \tag{60}$$

and loss of Nitrogen due to lysis reads

$$\hat{\lambda}^{lys}_N = N^{min}\hat{\lambda}^{lys}. \tag{61}$$

Silica, which is a key nutrient for diatoms growth due to its role in formation of cell walls follows the same structure where the nutrient is gained by uptake of inorganic silicates (I^{Si}) and lost due to detritus.

$$(C_{Si})' = \hat{\rho}^{upt}_{I^{Si}} - \hat{\lambda}^{lys}_{Si}, \tag{62}$$

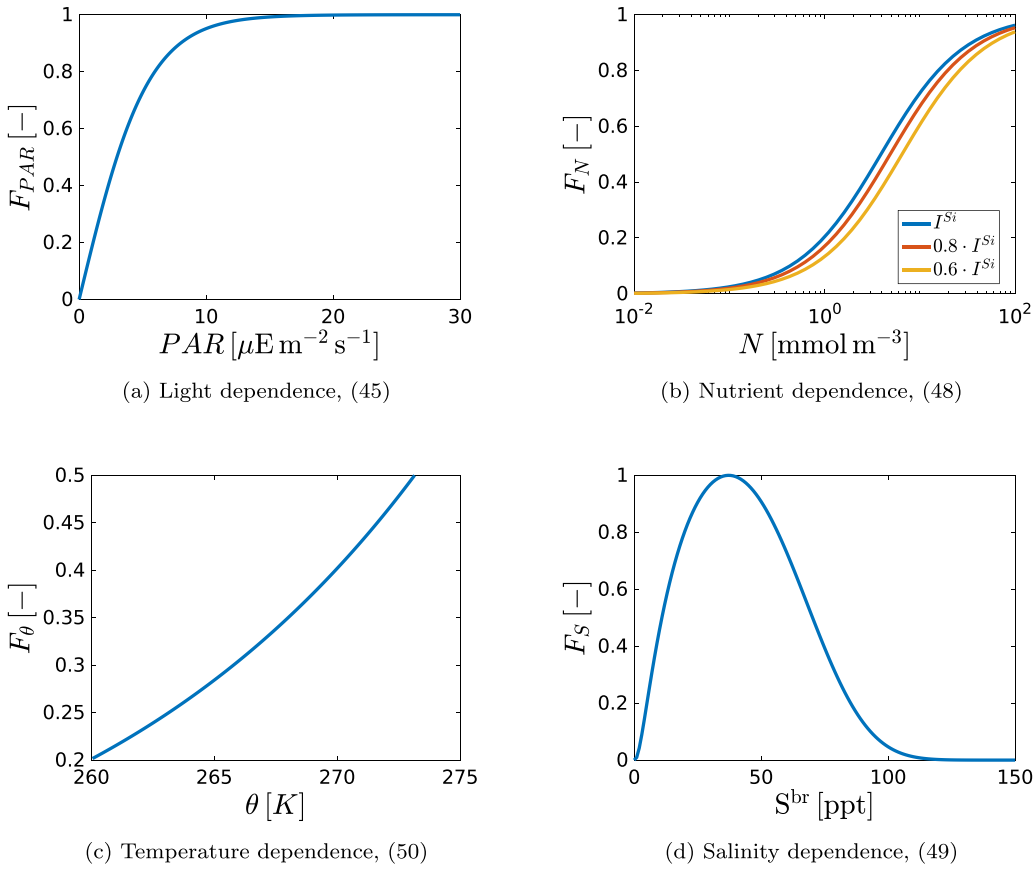

(a) Light dependence, (45)

(b) Nutrient dependence, (48)

(c) Temperature dependence, (50)

(d) Salinity dependence, (49)

Fig. 4. Environmental forcing functions.

where

$$\hat{\rho}^{upt}_{I^{Si}} = Si_{max} G, \quad \text{and} \quad \hat{\lambda}^{lys}_{Si} = \frac{C_{Si}}{C_C} \hat{\lambda}^{lys}. \tag{63}$$

The evolution of algal chlorophyll component $Chl - a$ is determined using a dynamic maximum photosynthesis potential θ_{Chl} as a factor associated with production and exudation losses and a dynamic chlorophyll to carbon ratio associated with respiration and lysis loss

$$\left(C_{Chl}\right)' = \theta_{Chl} \left(\hat{\rho}^{gpp} - \hat{\lambda}^{exu}_{det}\right) - \left(\hat{\lambda}^{res} + \hat{\lambda}^{lys}_{det}\right) \frac{C_{Chl}}{C_C}. \tag{64}$$

The symbols, reference values, description for various factors used in the modeling are given in Table 1.

Finally, a diagram is presented in Fig. 5 to summarize the micro and macroscale physics and the biogeochemical models and their coupled interactions with each other.

4. Results and discussion

This section presents simulation results of the described model. After a short overview on the description of the Initial Boundary Value Problem (IBVP), discussion on sea ice freezing is presented during winter and summer conditions. Next, a detailed discussion on photosynthesis, with two examples of seasonal conditions during summer and winter are shown. Finally, the section ends with results for year long monthly variations in photosynthetic activity, taking data from the literature (Henley et al., 2023a).

The IBVP is chosen to consider a realistic physical condition in the Southern Ocean, where a domain of seawater starts freezing from top due to lower atmospheric temperature. The domain is chosen to be able to appropriately describe macroscale and microscale processes. Results are plotted along the centerline as shown in Fig. 6.

Table 1
Description and values of parameters used in modeling primary production (Tedesco et al., 2012).

Symbol	Value	Description
$\hat{\rho}^{gpp}_{\max}$	1.5	Max. specific photosynthetic rate depending on ambient conditions $(\mathrm{d^{-1}})$
Q_{10}	2.0	Characteristic Q_{10} coefficient (–)
θ_{chl}	0.035	Opt. quotum $C_{Chl} : C_C$ (mg chl mg $\mathrm{C^{-1}}$)
α	$1.8 \cdot 10^{-3}$	Max. light utilization coef. $(\mathrm{mg\,C\,(mg\,chl)^{-1}\,mE^{-1}\ m^2\ s})$
d_{Si}	0.1	Half saturation value for Si -limitation $(\mathrm{mmol\,Si\,m^{-2}})$
b	0.05	Basal specific respiration rate $(\mathrm{d^{-1}})$
γ	0.1	Activity respiration fraction (–)
β	0.05	Excreted fraction of primary production (–)
$d^{p,n}$	0.1	Nutrient stress threshold (–)
d_0	0.1	Max. specific lysis rate $(\mathrm{d^{-1}})$
$a_{\mathrm{PO_4}}$	$2.5 \cdot 10^{-3}$	Specific affinity const., $P\,(\mathrm{m^{-2}\,mg\,C^{-1}\ d^{-1}})$
$a_{\mathrm{NO_3}}$	$2.5 \cdot 10^{-3}$	Specific affinity const., $\mathrm{N-NO_3}\,(\mathrm{m^{-2}\,mg\,C^{-1}\ d^{-1}})$
$a_{\mathrm{NH_4}}$	$2.5 \cdot 10^{-3}$	Specific affinity const., $\mathrm{N-NH_4}\,(\mathrm{m^{-2}\,mg\,C^{-1}\ d^{-1}})$
Si_{max}	0.085	Max. $Si : C$ ratio (mmol Si mg $\mathrm{C^{-1}}$)
P^{min}	$1.97 \cdot 10^{-4}$	Min. P quota $(\mathrm{mmol\,P\,mg\,C^{-1}})$
P^{opt}	$7.86 \cdot 10^{-4}$	Opt. P quota $(\mathrm{mmol\,P\,mg\,C^{-1}})$
P^{max}	$1.57 \cdot 10^{-4}$	Max. P quota $(\mathrm{mmol\,P\,mg\,C^{-1}})$
N^{min}	$3.78 \cdot 10^{-4}$	Min. N quota $(\mathrm{mmol\,N\,mg\,C^{-1}})$
N^{opt}	$1.26 \cdot 10^{-4}$	Opt. N quota $(\mathrm{mmol\,N\,mg\,C^{-1}})$
N^{max}	$2.52 \cdot 10^{-4}$	Max. N quota $(\mathrm{mmol\,N\,mg\,C^{-1}})$

4.1. Ice physics

A 1-d freezing simulation is set up on the microscale considering that the major direction of freezing in along the vertical z-axis of the domain due to maximum temperature gradient along the vertical direction based on lower atmospheric temperatures on the upper surface and relatively warmer ocean water. The initial condition is set assuming an equal distribution of ice and brine phase in the domain ($\mathrm{n^{I}_{micro}}$). Based

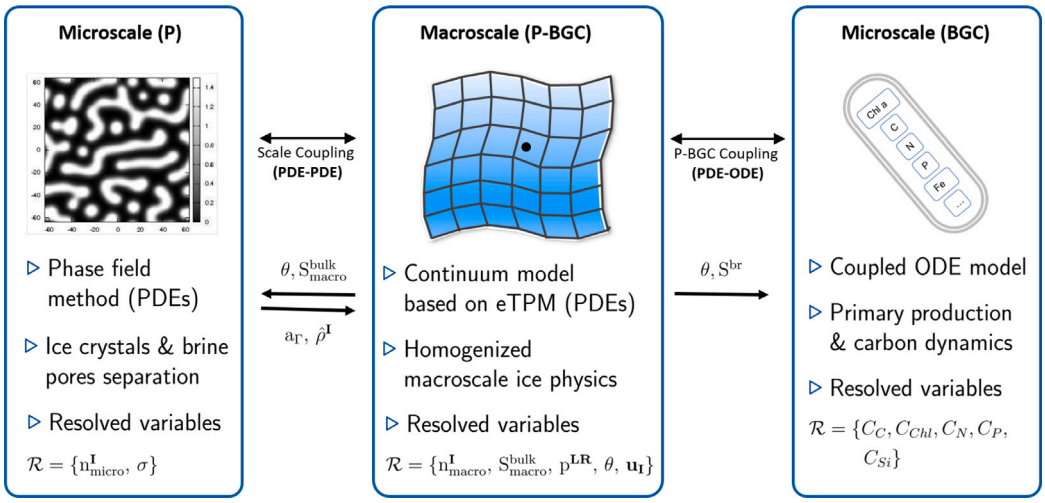

Fig. 5. Flowchart of models with their coupled interactions and the resolved variables.

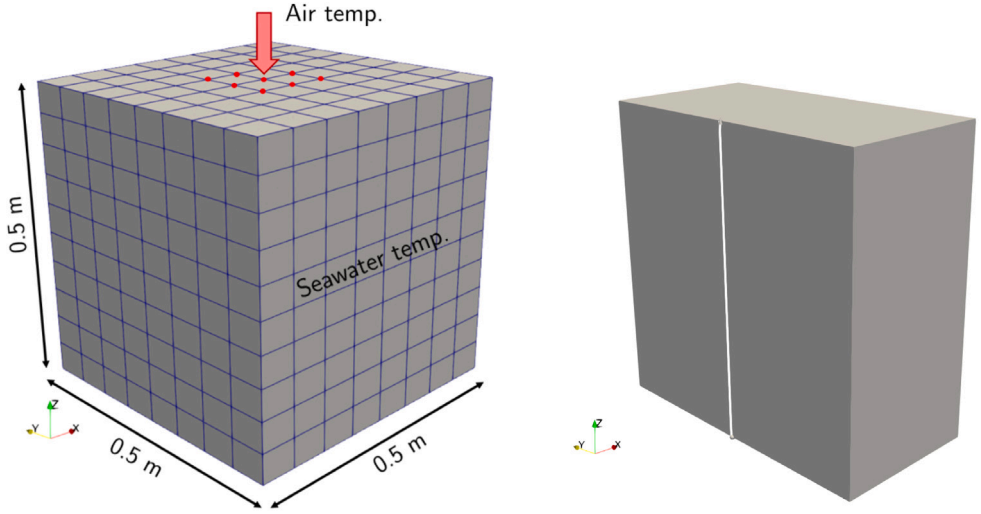

(a) Prescribed domain and BCs (b) Center line

Fig. 6. IBVP.

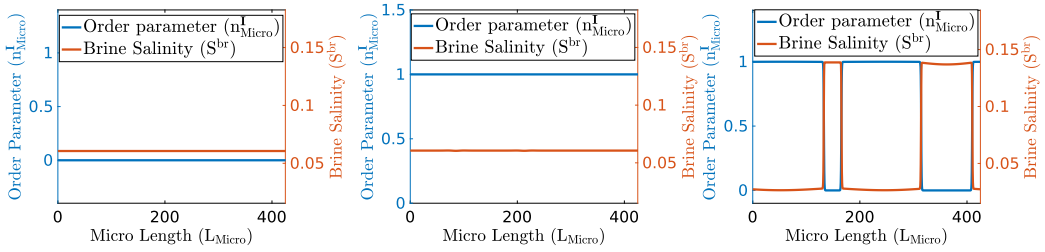

(a) $\theta = 273\,K, S^{bulk} = 35\frac{g}{kg}$ (b) $\theta = 265\,K, S^{bulk} = 35\frac{g}{kg}$ (c) $\theta = 270\,K, S^{bulk} = 35\frac{g}{kg}$

Fig. 7. Microscale phase field simulation.

on the bulk salinity and temperature, a completely ice filled, water filled or a mixed region with brine pore formation are reached at the equilibrium state using the coupled phase field model. Fig. 7 shows three different simulations for given ambient temperatures and bulk salinity.

Averaging over the length of the 1-d domain in Fig. 7(a), a pore diameter of $d_{pore} \approx 130\mu m$ is calculated from the ice free region, which is well in the range of observed brine channel sizes (Maus et al., 2021; Krembs et al., 2000). The modeled pore diameter also corroborates the choice of diatoms as a reasonable species to model within the sea ice matrix. On the macroscale, as shown in Fig. 6, for winter a

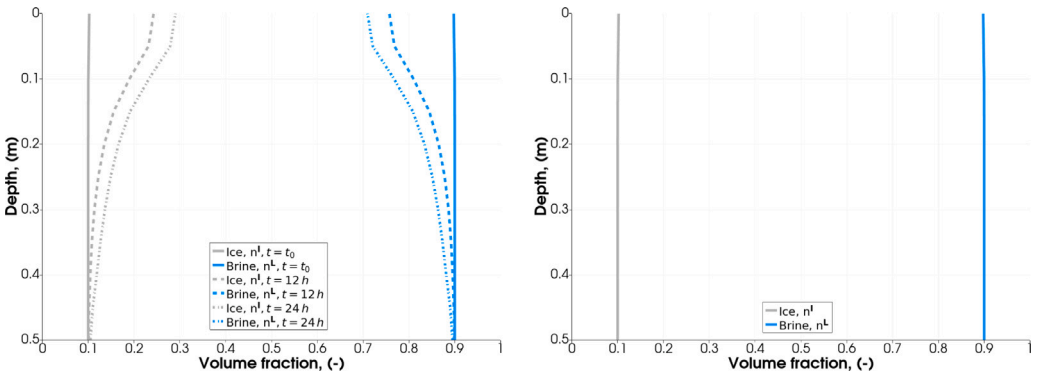

Fig. 8. Depth dependent ice volume fraction for winter (left) and summer (right) conditions.

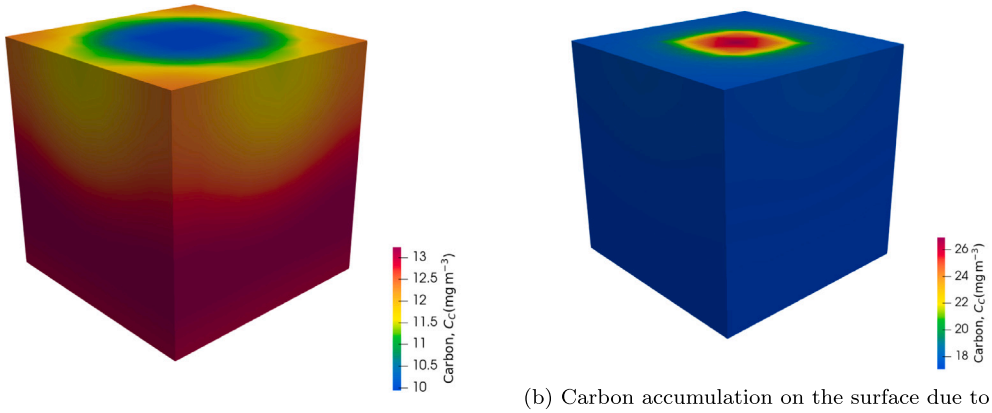

(a) Carbon accumulation under and around the ice, depicting presence of under ice communities

(b) Carbon accumulation on the surface due to high temperature and sunlight, depicting surface blooms

Fig. 9. Winter (left) and summer (right) dynamics of carbon assimilation.

temperature of $\theta = 263.15$ K is prescribed from the top and for summer, the prescribed temperature of $\theta = 272.15$ K. The time evolution of ice and brine volume fractions is shown in the following Fig. 8. Results for winter are shown on the left and for summer on the right, respectively.

The initial conditions on the ice volume fraction in both winter and summer conditions are chosen to be $n^I = 0.1$. This is considered primarily for two reasons. Firstly, a low value is chosen to depict the ice growth and the significant change in its amount during the winter months, and secondly, to observe the interaction between ice physics and BGC, some ice needs to be present in the domain also during the summer months. It can be observed clearly that the winter months are associated with an increase in the ice fraction, while in summers, there is no growth in ice. This plays an important role in the biogeochemical dynamics and associated algal primary productivity, as discussed in Section 4.2.

4.2. Ice BioGeoChemistry

The dynamic behavior of sea ice BGC is quite different over the annual cycle of seasons, as various environmental conditions influence it. In winter, the microbial communities use the ice floes to 'stick' and flourish at the ice ocean interface, known as under ice communities. In contrary, during summer, algal species grow on the surface of the ocean due to higher light availability and better temperature conditions, as shown in Fig. 9. The circular pattern occurring on the top surface is the region of prescribed Dirichlet boundary conditions of temperature. In physical conditions, this should be associated with the seawater surface interacting with contrasting atmospheric temperature. Starting from an initial carbon concentration of 10 mg m^{-3}, significantly higher carbon assimilation is observed during summer, growing as high as 26 mg m^{-3} compared to only about 13 mg m^{-3} during a typical day. For summer, even the regions of lowest concentrations of about 18 mg m^{-3} experience an increase from the initial condition. However, during winter the lowest concentration seems to be slightly lower than the initial condition, indicating a loss of carbon by algae potentially due to lysis. It must also be noted that the winter contour should not be perceived as a top-down growth. Rather, the growth is on the sides of the regions of minimum temperature, which can be associated with 'sticking' around the ice floes in physical conditions. This behavior is due to higher light availability in this region.

The environmental conditions cause the different functions to evolve and behave differently in both seasons. Assuming a constant incident sunlight and nutrients throughout the simulation, in winter, salinity and temperature have a negative influence on the overall primary production. In contrary, during summer, temperature has a positive behavior and increases production. Since there is either low level of, or no ice in summer, salinity is assumed to remain constant across the domain and hence can be neglected as a relevant environmental forcing factor for production. Although during the day, a constant PAR is prescribed in the domain, attenuation due to growing sea ice produces a gradient over the depth. In summer, on the other hand, sunlight is much more available and due to the absence of ice, the gradient is minute and $F_{PAR} \approx 1$ throughout the domain. The temporal evolution of environmental factors is shown in Fig. 10. It must be noted that the first time step for all results shows a very steep, almost non-physical jump in the values. This is due to the fact that the boundary condition has a contrasting value compared to initial conditions at the seawater. The fluctuation decays with time and the results are stable and accurate.

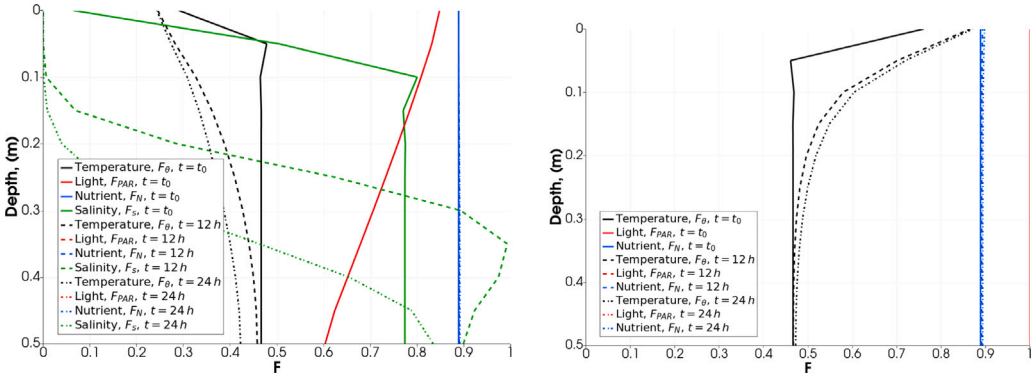

Fig. 10. Distribution of environmental functions over depth for winter (left) and summer (right) conditions.

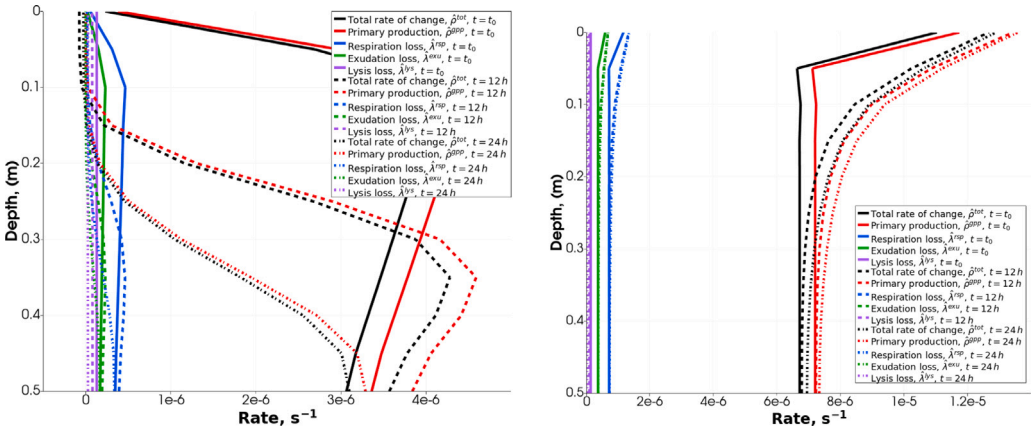

Fig. 11. Rates of physical mechanisms affecting carbon concentration for winter (left) and summer (right) conditions.

Primary production, however, is a byproduct of various growth and loss processes that involve carbon. The total carbon concentration change is dependent on the difference between the growth due to photosynthesis and losses due to respiration, exudation, and lysis. In winter, as the temperature and salinity evolve with time due to formation of ice, they become detrimental to algal growth. Respiration and exudation are directly dependent and follow photosynthesis. Lysis, however, increases at the top as the environmental conditions become adverse for the microbial communities. The total rate of change is then observed to increase initially but as the conditions worsen at the top, lysis overtakes photosynthesis and hence, decreases the total rate of change of carbon concentration. Fig. 11 show the dynamics of photosynthesis, respiration, exudation, and lysis and their effect on the total carbon assimilation rate.

Fig. 12 shows the evolution of carbon concentration starting from an initial condition of $C_C = 10\,\mathrm{mg\,m^{-3}}$. Due to lysis, it is seen that during winter the carbon concentration on the top layer decreases. An appropriate physical interpretation of this behavior can be related to the diatoms dying due to harsh temperature and salinity conditions on the top layers of ice. In the lower layers of sea ice, the carbon concentration initially increases because the conditions are favorable and after some time, starts to saturate. This is due to adverse temperature and salinity conditions also at the bottom due to growing ice. However, in summer, the temperature conditions are favorable and hence, the top layers observe maximum increase in carbon concentration. This can be corroborated to surface blooms observed in the MIZ when conditions are favorable.

It is also worth noting that the presented solutions present the initial phases of ice formation and algal dynamics within the sea ice system for short times that are still distant from the steady state conditions because it is a closed system and exchange of fluxes with atmosphere and ocean is not possible. This affects the carbon concentration, specially in summers, where it is observed to grow monotonically. Apart from this, efficient parametrization based on data is required to apply constraints that restrict the monotonic increase in carbon concentration. Incorporation of brine expulsion mechanisms from the sea ice matrix is also expected to further regulate the exchange of fluxes between the sea ice system and the ocean water. In the current model, constant PAR is assumed as an environmental variable. Incorporation of Gaussian like distributions that prescribe daylight conditions from sunrise to sunset can avoid such exponential growth curves, as seen on the plot for summer conditions.

4.3. Nutrients

The ratio of chlorophyll and carbon concentrations $C_{Chl} : C_C$ in diatoms is a determining parameter for the interplay between various environmental and ecological conditions (Wang et al., 2009; Yacobi and Zohary, 2010; Smyth et al., 2023). High $C_{Chl} : C_C$ ratios typically indicate low light environments and conditions, where diatom species increase their chlorophyll content to maximize the absorption of available PAR content for photosynthesis. While this is often associated with deeper waters, in winter other factors like low light availability, light attenuation due to sea ice, harsh temperature and salinity conditions, and low nutrient availability can also result in higher $C_{Chl} : C_C$ ratios. In surface water, it is common for diatoms to reduce their chlorophyll content, to avoid photodamage (Álvarez et al., 2018), and low $C_{Chl} : C_C$ ratios are typically suggestive of high light environments, such as typical summer conditions in MIZ. Fig. 13 shows the variation of $C_{Chl} : C_C$ ratios along height in two different seasonal conditions.

Fig. 14 indicates the overall actual chlorophyll and carbon concentrations along height are quite low in winter when compared to summer

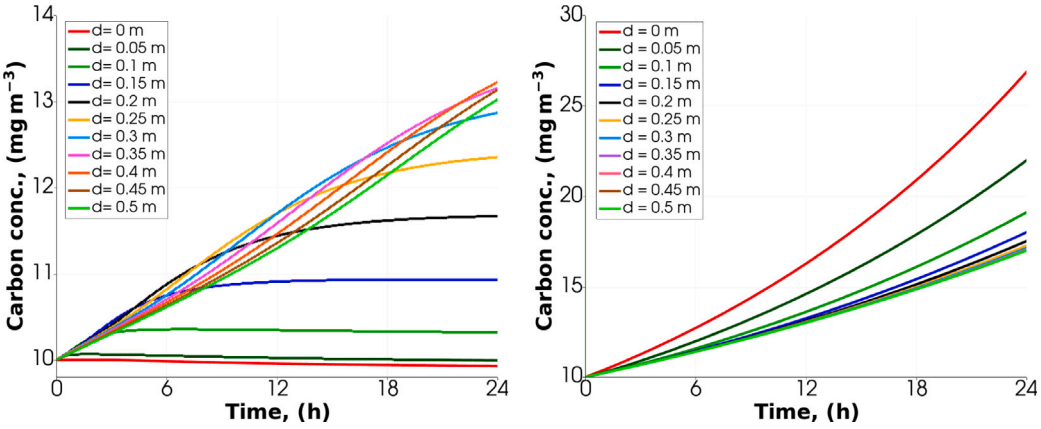

Fig. 12. Evolution of carbon concentration along depth for winter (left) and summer (right) conditions.

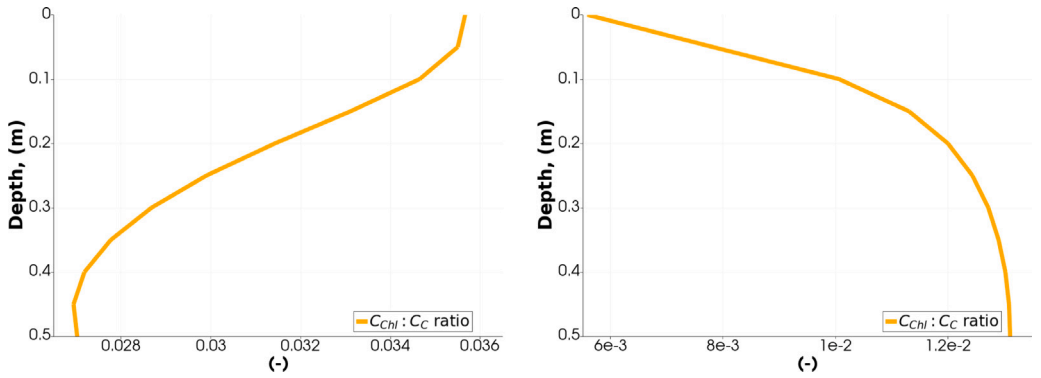

Fig. 13. Chlorophyll to carbon ratio for winter (left) and summer (right) conditions.

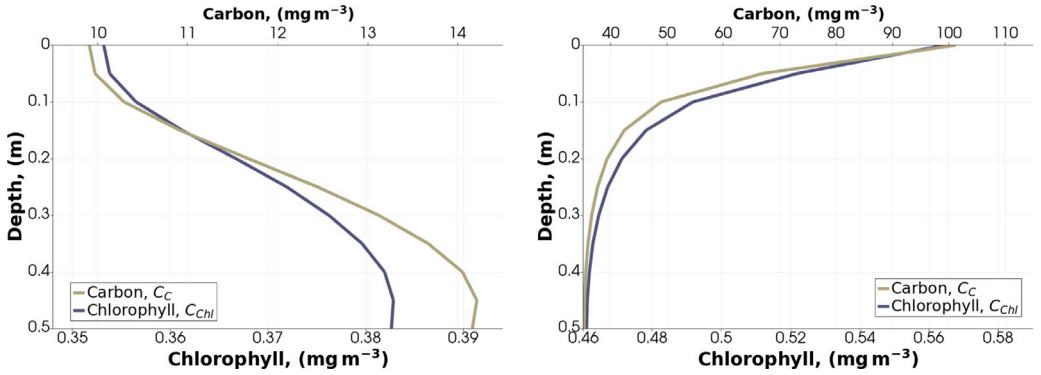

Fig. 14. Chlorophyll and carbon concentration for winter (left) and summer (right) conditions.

conditions. The unfavorable winter conditions keep the concentration levels low, despite projecting high $C_{Chl} : C_C$ ratios.

Although nutrients are assumed to be constant during a simulation run, a change in availability of nutrients is modeled, keeping other conditions constant. Silica, being an important nutrient for production of diatom cells, is analyzed. Fig. 15 shows a direct dependence of carbon concentration on silica. It is also observed that major shifts are seen only around optimal $C_{Si} : C_C$ ratio of $\approx 0.1\,\mathrm{mmol\,m^{-3}}$ and nutrient values further away from optimal ratios produce little differences in the carbon concentrations as shown for values of 10 and $100\,\mathrm{mmol\,m^{-3}}$.

4.4. Seasonal primary production

Once the key environmental variables are discussed in the contrasting seasonal settings, simulations are performed to describe seasonal variations in carbon concentrations over the period of a year. Henley et al. (2023b) presented a circumpolar compilation of publically available literature about macronutrient data around the Antarctic continent. Monthly values of air temperature, water temperature, PAR, and silicic acid are obtained from the paper for the model runs. The data considers surface flooding as an associated process and hence, distribution of the nutrient varies along height, cf. Table 2.

The initial conditions for the carbon and chlorophyll concentrations were set to $C_C = 10\,\mathrm{mg\,m^{-3}}$ and $C_{Chl} = 0.35\,\mathrm{mg\,m^{-3}}$ for each month, maintaining a chlorophyll to carbon ratio $C_{Chl} : C_C = 0.035$. Starting again with the environmental forcing functions, Fig. 16 shows the variations along height for each season of the forcing functions.

Fig. 17 presents the results for ice volume fraction and carbon concentration during one simulated day. The initial concentrations are denoted with dotted line and final concentrations for each month are

Table 2
Monthly distribution of key environmental variables.

Month	Air temp (°C)	Water temp (°C)	PAR ($\mu E\,m^2 s^{-1}$)	Si (μmol)		
				Top 0.1 m	Mid	Bottom 0.2 m
January	−2	−1.3	20.175	0.012	0.006	0.007
February	−3	−1.4	13.157	0.012	0.006	0.007
March	−6	−1.6	6.140	0.012	0.006	0.007
April	−10	−1.8	1.096	0.022	0.041	0.03
May	−12	−1.8	0.438	0.05	0.04	0.028
June	−14	−1.8	0.219	0.08	0.038	0.025
July	−16	−1.8	0.438	0.06	0.05	0.025
August	−16	−1.8	2.192	0.03	0.045	0.03
September	−14	−1.8	4.385	0.022	0.018	0.022
October	−11	−1.8	10.964	0.018	0.015	0.018
November	−6	−1.7	18.640	0.01	0.01	0.01
December	−3	−1.6	23.023	0.008	0.008	0.008

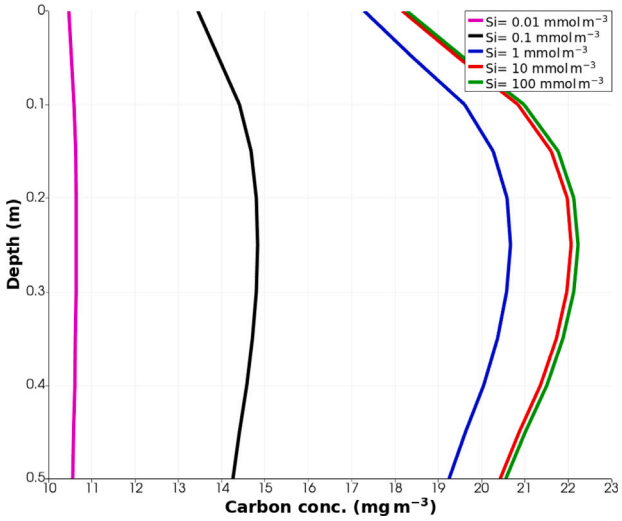

Fig. 15. Effect of Silica limitation on carbon concentration along depth.

plotted to show the evolution of the variable for each month. It can be seen that the months associated with Antarctic summer, October to February, exhibit high values of concentrations and the winter months from March to September have relatively low values. It is also worth noting that while the chlorophyll concentration increases in each month compared to its respective initial value, carbon concentrations for June and July are below the initial values, indicating predominance of lysis in those months. For the upper layers, except for months with very high PAR and favorable temperature, respectively in December, January, and February, the carbon concentration is below the initial value. As shown before in Fig. 12 for two contrasting conditions of summer and winter, the months associated with summer again tend to show a top-down algal growth while the months associated with winter show a bottom up algal growth.

While qualitative discussion on the evolution of various key physical and BGC variables has been the focus of discussion throughout the paper, the results have also been validated quantitatively as much as possible. However, due to lack of reliable data related to photosynthesis capacity of sea ice algae, direct validations are very difficult to be achieved. Due to shortage of observations about ice algae production, algal biomass is considered in most studies as a measure of primary production. However, algal biomass and production are only weekly correlated (Pinkerton and Hayward, 2021). Ice algae living within the brine channels in sea ice are invisible to satellites, which are typically the drivers of climate research data (Lieser et al., 2015). This further adds to the challenge of reliable data availability. Available observation methods like ice core extraction and measurement of biomass provide only instantaneous values of concentrations, rather than temporal information on the growth and loss rates. Quantifying methods of under-ice biomass and production through autonomous remote sensing vehicles have recently been developed (Cimoli et al., 2017; Meiners et al., 2017). Even though homogenization based mathematical models are really effective to model heterogeneous materials like the sea ice and its associated processes and are often computationally cheaper than running full scale high-fidelity simulations, the smearing out of the process variables over the domain often make them incomparable with traditionally available observation data. The research group also plans to design and carry out their own experiments that are co-developed with close interactions and inputs with the current state of the mathematical model. This will yield data in controlled environments that can help in effectively validating the model. Evolution of key variables like temperature, ice and brine volume fraction with salinity distribution will be studied over time. Reproduction of the experimental setup virtually with the mathematical model will serve as a validation. These developments could help in future to validate temporal and spatial evolution of BGC variables.

5. Conclusion

This paper presents an approach to model coupled seasonal Physical–BioGeoChemical processes associated with sea ice in the Marginal Ice Zone. A one way coupling of environmental forcing functions associated with BioGeoChemistry is derived from the physical variables of temperature and salinity, resolved using extended Theory of Porous Media. The temporal dynamics of environmental conditions during different seasons is modeled and discussed in detail to understand their effect on primary production and nutrient mobility. Diatom winter adaptation is shown through chlorophyll to carbon $C_{Chl} : C_C$ ratio. Finally, a typical season in the Southern Ocean is modeled using environmental data from literature to show potential trends in the annual primary production in the marginal ice zone. The results are well in permissible ranges of values observed in reality. However, a direct quantitative validation has not been achieved in this paper owing to the fact that both a consensus and availability of data associated with small scale coupled P-BGC processes in sea ice obtained through non-intrusive observation methods is still lacking. This approach, hence, is aimed at facilitating in the understanding of such critical and complex processes occurring in rather inaccessible conditions. Ecosystem models will also be developed and coupled, considering top-down dynamics and their effects on the carbon assimilation.

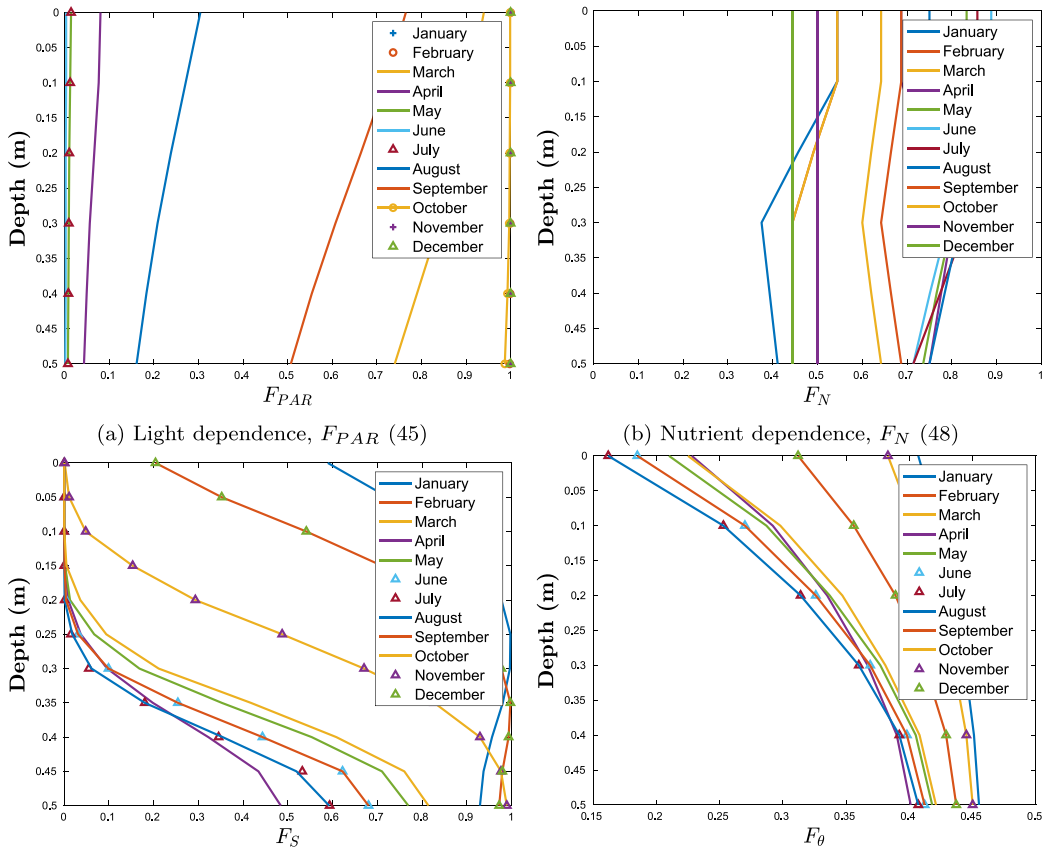

(a) Light dependence, F_{PAR} (45) (b) Nutrient dependence, F_N (48)

(c) Salinity dependence, F_s (49) (d) Temperature dependence, F_θ (50)

Fig. 16. Monthly variations in the initial conditions over depth.

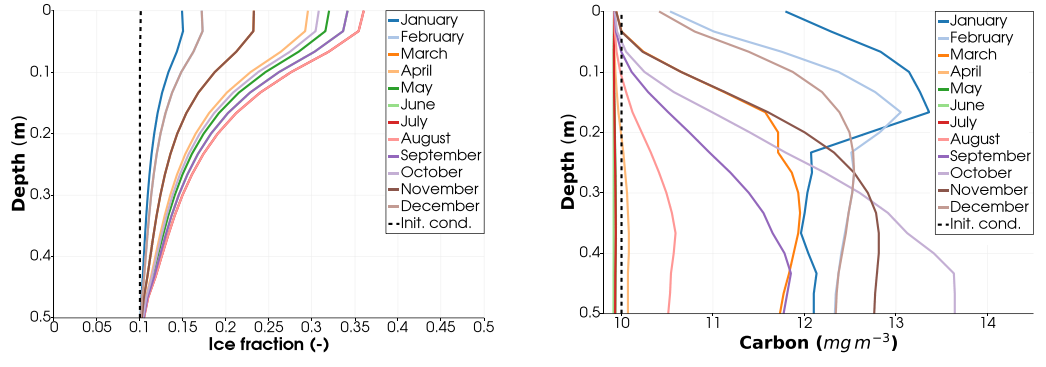

(a) Ice fraction, n^{I} (b) Carbon concentration, C_C

Fig. 17. Seasonal dynamics during a 24 h simulation.

CRediT authorship contribution statement

Raghav Pathak: Conceptualization, Methodology, Formal analysis, Investigation, Writing – review & editing, Writing – original draft, Software. **Seyed Morteza Seyedpour:** Writing – review & editing, Writing – original draft, Supervision, Conceptualization. **Bernd Kutschan:** Writing – review & editing, Methodology, Conceptualization. **Silke Thoms:** Writing – review & editing, Supervision, Conceptualization. **Tim Ricken:** Supervision, Project administration, Conceptualization.

Declaration of competing interest

The authors declare that they have no known competing financial interests or personal relationships that could have appeared to influence the work reported in this paper.

Acknowledgments

This work was supported by the Deutsche Forschungsgemeinschaft, Germany (DFG) in the framework of the priority program SPP 1158

"Antarctic Research with comparative investigations in Arctic ice areas" by the following grant 463296570 (Priority Programme SPP 1158, Antarctica). T.R. further thanks the Deutsche Forschungsgemeinschaft, Germany (DFG, German Research Foundation) for supporting this work via the following projects: 312860381 (Priority Program SPP 1886, Subproject 12); 390740016 (Germany's Excellence Strategy EXC 2075/1); 436883643 (Research Unit Programme FOR 5151 (QuaLiPerF), Project P7); 327154368 (SFB 1313 Project C03 Vertebroplasty); 504766766 (Project Hybrid MOR); 465194077 (Priority Programme SPP 2311, Project SimLivA). TR is further supported by the Federal Ministry of Education and Research (BMBF, Germany) within ATLAS by grant number 031L0304A. RP is supported by the Add-on Fellowship of the Joachim Herz Foundation.

Data availability

Data will be made available on request.

References

Álvarez, E., Thoms, S., Völker, C., 2018. Chlorophyll to carbon ratio derived from a global ecosystem model with photodamage. Glob. Biogeochem. Cycles 32 (5), 799–816. http://dx.doi.org/10.1029/2017GB005850.

Arrigo, K.R., 2017. Sea ice as a habitat for primary producers. In: Sea Ice. John Wiley & Sons, Ltd, pp. 352–369. http://dx.doi.org/10.1002/9781118778371.ch14, Chapter 14.

Arrigo, K.R., Mock, T., Lizotte, M.P., 2009. Primary producers and sea ice. In: Thomas, D.N., Dieckmann, G.S. (Eds.), Sea Ice, first ed. Wiley, pp. 283–325. http://dx.doi.org/10.1002/9781444317145.ch8, URL https://onlinelibrary.wiley.com/doi/10.1002/9781444317145.ch8.

Arrigo, K.R., Sullivan, C.W., 1992. The influence of salinity and temperature covariation on the photophysiological characteristics of Antarctic sea ice microalgae [1]. J. Phycol. 28 (6), 746–756. http://dx.doi.org/10.1111/j.0022-3646.1992.00746.x, URL https://onlinelibrary.wiley.com/doi/10.1111/j.0022-3646.1992.00746.x.

Arrigo, K.R., Thomas, D.N., 2004. Large scale importance of sea ice biology in the Southern Ocean. Antarctic Sci. 16 (4), 471–486. http://dx.doi.org/10.1017/S0954102004002263, URL https://www.cambridge.org/core/product/identifier/S0954102004002263/type/journal_article.

Arrigo, K.R., Van Dijken, G.L., 2003. Phytoplankton dynamics within 37 Antarctic coastal polynya systems. J. Geophys. Res.: Oceans 108 (C8), 2002JC001739. http://dx.doi.org/10.1029/2002JC001739, URL https://agupubs.onlinelibrary.wiley.com/doi/10.1029/2002JC001739.

Bluhm, J., Bloßfeld, W., Ricken, T., 2014. Energetic effects during phase transition under freezing-thawing load in porous media – a continuum multiphase description and FE-simulation. Z. Angew. Math. Mech. 94 (7–8), 586–608. http://dx.doi.org/10.1002/zamm.201200154, URL https://onlinelibrary.wiley.com/doi/10.1002/zamm.201200154.

Bluhm, J., Ricken, T., Bloßfeld, W.M., 2009. Freezing and thawing processes in porous media – Experiment and Simulation. Proc. Appl. Math. Mech. 9 (1), 387–388. http://dx.doi.org/10.1002/pamm.200910167, URL https://onlinelibrary.wiley.com/doi/10.1002/pamm.200910167.

Bowen, R.M., 1969. The thermochemistry of a reacting mixture of elastic materials with diffusion. Arch. Ration. Mech. Anal. 34, 97–127. http://dx.doi.org/10.1007/BF00247461.

Bryceson, K.P., Leigh, S., Sarwar, S., Grøndahl, L., 2022. Affluent effluent: Visualizing the invisible during the development of an algal bloom using systems dynamics modelling and augmented reality technology. Environ. Model. Softw. 147, 105253. http://dx.doi.org/10.1016/j.envsoft.2021.105253, URL https://www.sciencedirect.com/science/article/pii/S1364815221002954.

Cimoli, E., Meiners, K., Lund-Hansen, L., Lucieer, V., 2017. Spatial variability in sea-ice algal biomass: an under-ice remote sensing perspective. Adv. Polar Sci. 28, http://dx.doi.org/10.13679/j.advps.2017.4.00268.

Cox, S., Matthews, P., 2002. Exponential time differencing for stiff systems. J. Comput. Phys. 176 (2), 430–455. http://dx.doi.org/10.1006/jcph.2002.6995, URL https://www.sciencedirect.com/science/article/pii/S0021999102969950.

Dawson, H.M., Connors, E., Erazo, N.G., Sacks, J.S., Mierzejewski, V., Rundell, S.M., Carlson, L.T., Deming, J.W., Ingalls, A.E., Bowman, J.S., Young, J.N., 2023. Microbial metabolomic responses to changes in temperature and salinity along the western Antarctic Peninsula. ISME J. 17 (11), 2035–2046. http://dx.doi.org/10.1038/s41396-023-01475-0, URL https://academic.oup.com/ismej/article/17/11/2035-2046/7505877.

de Boer, R., 1996. Highlights in the historical development of the porous media theory: Toward a consistent macroscopic theory. Appl. Mech. Rev. 49 (4), 201–262. http://dx.doi.org/10.1115/1.3101926, URL https://asmedigitalcollection.asme.org/appliedmechanicsreviews/article/49/4/201/401138/Highlights-in-the-Historical-Development-of-the.

de Boer, R., Bluhm, J., 1999. Phase transitions in gas- and liquid-saturated porous solids. Transp. Porous Media 34 (1/3), 249–267. http://dx.doi.org/10.1023/A:1006577828659, URL http://link.springer.com/10.1023/A:1006577828659.

Drumheller, D.S., 1978. The theoretical treatment of a porous solid using a mixture theory. Int. J. Solids Struct. 14 (6), 441–456. http://dx.doi.org/10.1016/0020-7683(78)90009-4.

Ehlers, W., 2002. Foundations of multiphasic and porous materials. In: Ehlers, W., Bluhm, J. (Eds.), Porous Media. Springer Berlin Heidelberg, Berlin, Heidelberg, pp. 3–86. http://dx.doi.org/10.1007/978-3-662-04999-0_1, URL http://link.springer.com/10.1007/978-3-662-04999-0_1.

Ehlers, W., Bluhm, J., 2011. Porous Media: Theory, Experiments and Numerical Applications. Springer, Berlin, OCLC: 751579205.

Falkowski, P.G., Knoll, A.H. (Eds.), 2007. Evolution of Primary Producers in the Sea. Elsevier Academic Press, Amsterdam ; Boston, OCLC: ocn145431763.

Fischer, W.W., Hemp, J., Johnson, J.E., 2016. Evolution of oxygenic photosynthesis. Annu. Rev. Earth Planet. Sci. 44 (1), 647–683. http://dx.doi.org/10.1146/annurev-earth-060313-054810, URL https://www.annualreviews.org/doi/10.1146/annurev-earth-060313-054810.

Grossi, S.M., Kottmeier, S.T., Moe, R.L., Taylor, G.T., Sullivan, C.W., 1987. Sea ice microbial communities. VI. Growth and primary production in bottom ice under graded snow cover. Mar. Ecol. Prog. Ser. 35 (1/2), 153–164, Publisher: Inter-Research Science Center, URL http://www.jstor.org/stable/24825019.

Gürses, Ö., Oziel, L., Karakuş, O., Sidorenko, D., Völker, C., Ye, Y., Zeising, M., Butzin, M., Hauck, J., 2023. Ocean biogeochemistry in the coupled ocean–sea ice–biogeochemistry model FESOM2.1–REcoM3. Geosci. Model Dev. 16 (16), 4883–4936. http://dx.doi.org/10.5194/gmd-16-4883-2023, URL https://gmd.copernicus.org/articles/16/4883/2023/.

Hassanizadeh, M., Gray, W.G., 1979a. General conservation equations for multi-phase systems: 1. Averaging procedure. Adv. Water Resour. 2, 131–144. http://dx.doi.org/10.1016/0309-1708(79)90025-3.

Hassanizadeh, M., Gray, W.G., 1979b. General conservation equations for multi-phase systems: 2. Mass, momenta, energy, and entropy equations. Adv. Water Resour. 2, 191–203. http://dx.doi.org/10.1016/0309-1708(79)90035-6.

Henley, S.F., Cozzi, S., Fripiat, F., Lannuzel, D., Nomura, D., Thomas, D.N., Meiners, K.M., Vancoppenolle, M., Arrigo, K., Stefels, J., van Leeuwe, M., Moreau, S., Jones, E.M., Fransson, A., Chierici, M., Delille, B., 2023a. Macronutrient biogeochemistry in Antarctic land-fast sea ice: Insights from a circumpolar data compilation. Mar. Chem. 257, 104324. http://dx.doi.org/10.1016/j.marchem.2023.104324, URL https://www.sciencedirect.com/science/article/pii/S0304420323001202.

Henley, S.F., Cozzi, S., Fripiat, F., Lannuzel, D., Nomura, D., Thomas, D.N., Meiners, K.M., Vancoppenolle, M., Arrigo, K., Stefels, J., Van Leeuwe, M., Moreau, S., Jones, E.M., Fransson, A., Chierici, M., Delille, B., 2023b. Macronutrient biogeochemistry in Antarctic land-fast sea ice: Insights from a circumpolar data compilation. Mar. Chem. 257, 104324. http://dx.doi.org/10.1016/j.marchem.2023.104324, URL https://linkinghub.elsevier.com/retrieve/pii/S0304420323001202.

Kirst, G.O., Wiencke, C., 1995. Ecophysiology of polar algae. J. Phycol. 31 (2), 181–199. http://dx.doi.org/10.1111/j.0022-3646.1995.00181.x, URL https://onlinelibrary.wiley.com/doi/10.1111/j.0022-3646.1995.00181.x.

Koh, E., Martin, A., McMinn, A., Ryan, K., 2012. Recent advances and future perspectives in microbial phototrophy in Antarctic Sea Ice. Biology 1, 542–556. http://dx.doi.org/10.3390/biology1030542.

Kohlbach, D., Lange, B.A., Schaafsma, F.L., David, C., Vortkamp, M., Graeve, M., Van Franeker, J.A., Krumpen, T., Flores, H., 2017. Ice algae-produced carbon is critical for overwintering of Antarctic Krill Euphausia superba. Front. Mar. Sci. 4, 310. http://dx.doi.org/10.3389/fmars.2017.00310, URL http://journal.frontiersin.org/article/10.3389/fmars.2017.00310/full.

Krembs, C., Eicken, H., Junge, K., Deming, J., 2002. High concentrations of exopolymeric substances in Arctic winter sea ice: implications for the polar ocean carbon cycle and cryoprotection of diatoms. Deep Sea Res. Part I: Oceanographic Res. Pap. 49 (12), 2163–2181. http://dx.doi.org/10.1016/S0967-0637(02)00122-X, URL https://linkinghub.elsevier.com/retrieve/pii/S096706370200122X.

Krembs, C., Gradinger, R., Spindler, M., 2000. Implications of brine channel geometry and surface area for the interaction of sympagic organisms in Arctic sea ice. J. Exp. Mar. Biol. Ecol. 243 (1), 55–80. http://dx.doi.org/10.1016/S0022-0981(99)00111-2, URL https://www.sciencedirect.com/science/article/pii/S0022098199001112.

Landschützer, P., Gruber, N., Bakker, D.C.E., 2016. Decadal variations and trends of the global ocean carbon sink. Glob. Biogeochem. Cycles 30 (10), 1396–1417. http://dx.doi.org/10.1002/2015GB005359, URL https://agupubs.onlinelibrary.wiley.com/doi/10.1002/2015GB005359.

Lewis, R.W., Schrefler, B.A., 1999. The Finite Element Method in the Static and Dynamic Deformation and Consolidation of Porous Media. John Wiley & Sons, Chinchester.

Lieser, J.L., Curran, M.A.J., Bowie, A.R., Davidson, A.T., Doust, S.J., Fraser, A.D., Galton-Fenzi, B.K., Massom, R.A., Meiners, K.M., Melbourne-Thomas, J., Reid, P.A., Strutton, P.G., Vance, T.R., Vancoppenolle, M., Westwood, K.J., Wright, S.W., 2015. Antarctic slush-ice algal accumulation not quantified through conventional satellite imagery: Beware the ice of march. Cryosphere Discuss. 9, 6187–6222. http://dx.doi.org/10.5194/tcd-9-6187-2015, URL https://tc.copernicus.org/preprints/9/6187/2015/.

Malve, O., Laine, M., Haario, H., Kirkkala, T., Sarvala, J., 2007. Bayesian modelling of algal mass occurrences—using adaptive MCMC methods with a lake water quality model. Environ. Model. Softw. 22 (7), 966–977. http://dx.doi.org/10.1016/j.envsoft.2006.06.016, URL https://www.sciencedirect.com/science/article/pii/S1364815206001599.

Manteaux, S., Sauvage, S., Samie, R., Monteil, C., Garnier, J., Thieu, V., Cakir, R., Sánchez-Pérez, J.-M., 2023. Modeling in-stream biogeochemical processes at catchment scale: Coupling SWAT and RIVE models. Environ. Model. Softw. 170, 105856. http://dx.doi.org/10.1016/j.envsoft.2023.105856, URL https://www.sciencedirect.com/science/article/pii/S1364815223002426.

Martinson, D.G., 2018. Antarctic Sea ice and global warming. In: Our Warming Planet. World Scientific, pp. 309–327. http://dx.doi.org/10.1142/9789813148796_0015, URL http://www.worldscientific.com/doi/abs/10.1142/9789813148796_0015.

Maus, S., Schneebeli, M., Wiegmann, A., 2021. An X-ray micro-tomographic study of the pore space, permeability and percolation threshold of young sea ice. Cryosphere 15 (8), 4047–4072. http://dx.doi.org/10.5194/tc-15-4047-2021, URL https://tc.copernicus.org/articles/15/4047/2021/.

McElroy, M.B., 1983. Marine biological controls on atmospheric CO2 and climate. Nature 302 (5906), 328–329. http://dx.doi.org/10.1038/302328a0, URL https://www.nature.com/articles/302328a0.

Meiners, K.M., Arndt, S., Bestley, S., Krumpen, T., Ricker, R., Milnes, M., Newbery, K., Freier, U., Jarman, S., King, R., Proud, R., Kawaguchi, S., Meyer, B., 2017. Antarctic pack ice algal distribution: Floe-scale spatial variability and predictability from physical parameters. Geophys. Res. Lett. 44 (14), 7382–7390. http://dx.doi.org/10.1002/2017GL074346.

Moj, L., Foppe, M., Deike, R., Ricken, T., 2017. Micro-macro modelling of steel solidification: A continuum mechanical, bi-phasic, two-scale model including thermal driven phase transition. GAMM-Mitt. 40 (2), 125–137. http://dx.doi.org/10.1002/gamm.201720004, URL https://onlinelibrary.wiley.com/doi/10.1002/gamm.201720004.

Notz, D., Worster, M.G., 2009. Desalination processes of sea ice revisited. J. Geophys. Res. 114 (C5), 2008JC004885. http://dx.doi.org/10.1029/2008JC004885, URL https://agupubs.onlinelibrary.wiley.com/doi/10.1029/2008JC004885.

Pardo, P.C., Tilbrook, B., Langlais, C., Trull, T.W., Rintoul, S.R., 2017. Carbon uptake and biogeochemical change in the Southern Ocean, south of Tasmania. Biogeosciences 14 (22), 5217–5237. http://dx.doi.org/10.5194/bg-14-5217-2017, URL https://bg.copernicus.org/articles/14/5217/2017/.

Passman, S., 1977. Mixtures of granular materials. Internat. J. Engrg. Sci. 15 (2), 117–129. http://dx.doi.org/10.1016/0020-7225(77)90027-1.

Pinkerton, M.H., Hayward, A., 2021. Estimating variability and long-term change in sea ice primary productivity using a satellite-based light penetration index. J. Mar. Syst. 221, 103576. http://dx.doi.org/10.1016/j.jmarsys.2021.103576, URL https://www.sciencedirect.com/science/article/pii/S0924796321000749.

Pyo, J., Pachepsky, Y.A., Kim, M., Baek, S.-S., Lee, H., Cha, Y., Park, Y., Cho, K.H., 2019. Simulating seasonal variability of phytoplankton in stream water using the modified SWAT model. Environ. Model. Softw. 122, 104073. http://dx.doi.org/10.1016/j.envsoft.2017.11.005, URL https://www.sciencedirect.com/science/article/pii/S1364815216307381.

Ricken, T., Bluhm, J., 2010a. Modeling fluid saturated porous media under frost attack. GAMM-Mitt. 33 (1), 40–56. http://dx.doi.org/10.1002/gamm.201010004, URL https://onlinelibrary.wiley.com/doi/10.1002/gamm.201010004.

Ricken, T., Bluhm, J., 2010b. Remodeling and growth of living tissue: a multiphase theory. Arch. Appl. Mech. 80 (5), 453–465. http://dx.doi.org/10.1007/s00419-009-0383-1, URL http://link.springer.com/10.1007/s00419-009-0383-1.

Ricken, T., Sindern, A., Bluhm, J., Widmann, R., Denecke, M., Gehrke, T., Schmidt, T., 2014. Concentration driven phase transitions in multiphase porous media with application to methane oxidation in landfill cover layers. Z. Angew. Math. Mech. 94 (7–8), 609–622. http://dx.doi.org/10.1002/zamm.201200198, URL https://onlinelibrary.wiley.com/doi/10.1002/zamm.201200198.

Ricken, T., Thom, A., Gehrke, T., Denecke, M., Widmann, R., Schulte, M., Schmidt, T.C., 2020. Biological driven phase transitions in fully or partly saturated porous media: A multi-component fem simulation based on the theory of porous media. In: Giovine, P., Mariano, P.M., Mortara, G. (Eds.), In: Views on Microstructures in Granular Materials, vol. 44, Springer International Publishing, Cham, pp. 157–183. http://dx.doi.org/10.1007/978-3-030-49267-0_8, URL http://link.springer.com/10.1007/978-3-030-49267-0_8. Series Title: Advances in Mechanics and Mathematics.

Sabine, C.L., Feely, R.A., Gruber, N., Key, R.M., Lee, K., Bullister, J.L., Wanninkhof, R., Wong, C.S., Wallace, D.W.R., Tilbrook, B., Millero, F.J., Peng, T.H., Kozyr, A., Ono, T., Rios, A.F., 2004. The oceanic sink for anthropogenic CO $_2$. Science 305 (5682), 367–371. http://dx.doi.org/10.1126/science.1097403, URL https://www.science.org/doi/10.1126/science.1097403.

Schourup-Kristensen, V., Sidorenko, D., Wolf-Gladrow, D.A., Völker, C., 2014. A skill assessment of the biogeochemical model REcoM2 coupled to the finite element sea ice–ocean model (FESOM 1.3). Geosci. Model Dev. 7 (6), 2769–2802. http://dx.doi.org/10.5194/gmd-7-2769-2014, URL https://gmd.copernicus.org/articles/7/2769/2014/.

Schwarz, A., Bluhm, J., Schröder, J., 2020. Modeling of freezing processes of ice floes within the framework of the TPM. Acta Mech. 231 (8), 3099–3121. http://dx.doi.org/10.1007/s00707-020-02686-8, URL https://link.springer.com/10.1007/s00707-020-02686-8.

Schwarz, A., Bluhm, J., Schröder, J., 2021. Investigations on modeling of freezing processes within the framework of the theory of porous media. Proc. Appl. Math. Mech. 20 (1), e202000251. http://dx.doi.org/10.1002/pamm.202000251, URL https://onlinelibrary.wiley.com/doi/10.1002/pamm.202000251.

Seyedpour, S.M., Henning, C., Kirmizakis, P., Herbrandt, S., Ickstadt, K., Doherty, R., Ricken, T., 2023a. Uncertainty with varying subsurface permeabilities reduced using coupled random field and extended theory of porous media contaminant transport models. Water 15 (1), http://dx.doi.org/10.3390/w15010159, URL https://www.mdpi.com/2073-4441/15/1/159.

Seyedpour, S., Nafisi, S., Nabati, M., Pierce, D., Reichenbach, J., Ricken, T., 2022. Magnetic resonance imaging–based biomechanical simulation of cartilage: A systematic review. J. Mech. Behav. Biomed. Mater. 126, 104963. http://dx.doi.org/10.1016/j.jmbbm.2021.104963, URL https://www.sciencedirect.com/science/article/pii/S1751616121005932.

Seyedpour, S.M., Thom, A., Ricken, T., 2023b. Simulation of contaminant transport through the vadose zone: A continuum mechanical approach within the framework of the extended theory of porous media (eTPM). Water 15 (2), http://dx.doi.org/10.3390/w15020343, URL https://www.mdpi.com/2073-4441/15/2/343.

Smyth, T., Moffat, D., Tarran, G., Sathyendranath, S., Ribalet, F., Casey, J., 2023. Determining drivers of phytoplankton carbon to chlorophyll ratio at Atlantic Basin scale. Front. Mar. Sci. 10, 1191216. http://dx.doi.org/10.3389/fmars.2023.1191216, URL https://www.frontiersin.org/articles/10.3389/fmars.2023.1191216/full.

Tedesco, L., Vichi, M., 2010. BFM-SI: a new implementation of the biogeochemical flux model in sea ice. CMCC Res. Pap. http://dx.doi.org/10.2139/ssrn.1633366.

Tedesco, L., Vichi, M., Haapala, J., Stipa, T., 2010. A dynamic biologically active layer for numerical studies of the sea ice ecosystem. Ocean Model. 35 (1–2), 89–104. http://dx.doi.org/10.1016/j.ocemod.2010.06.008, URL https://linkinghub.elsevier.com/retrieve/pii/S1463500310001010.

Tedesco, L., Vichi, M., Thomas, D.N., 2012. Process studies on the ecological coupling between sea ice algae and phytoplankton. Ecol. Model. 226, 120–138. http://dx.doi.org/10.1016/j.ecolmodel.2011.11.011, URL https://linkinghub.elsevier.com/retrieve/pii/S0304380011005400.

Thom, A., Ricken, T., 2019. Towards a physical model of Antarctic sea ice microstructure including biogeochemical processes using the extended theory of porous media. Proc. Appl. Math. Mech. 19 (1), e201900285. http://dx.doi.org/10.1002/pamm.201900285, URL https://onlinelibrary.wiley.com/doi/10.1002/pamm.201900285.

Thom, A., Ricken, T., 2021. In silico modeling of coupled physical-biogeochemical (P-BGC) processes in Antarctic Sea Ice. Proc. Appl. Math. Mech. 20 (1), e202000308. http://dx.doi.org/10.1002/pamm.202000308, URL https://onlinelibrary.wiley.com/doi/10.1002/pamm.202000308.

Thomas, D.N. (Ed.), 2017. Sea ice, third ed. John Wiley & Sons, Chichester, UK ; Hoboken, NJ.

Thomas, D.N., Dieckmann, G.S., 2002. Antarctic sea ice–a habitat for extremophiles. Science 295 (5555), 641–644. http://dx.doi.org/10.1126/science.1063391, URL https://www.science.org/doi/10.1126/science.1063391.

Thomas, D.N., Dieckmann, G., 2010. Sea ice, second ed. Wiley-Blackwell, Oxford, OCLC: 520990387.

Thoms, S., Kutschan, B., Morawetz, K., 2014. Phase-field theory of brine entrapment in sea ice: Short-time frozen microstructures. arXiv:1405.0304.

Truesdell, C., 1984. Thermodynamics of homogeneous processes. In: Rational Thermodynamics. Springer New York, New York, NY, pp. 59–81. http://dx.doi.org/10.1007/978-1-4612-5206-1_3.

Volk, T., Hoffert, M.I., 2013. Ocean carbon pumps: Analysis of relative strengths and efficiencies in ocean-driven atmospheric CO $_2$ changes. In: Sundquist, E., Broecker, W. (Eds.), Geophysical Monograph Series. American Geophysical Union, Washington, D. C., pp. 99–110. http://dx.doi.org/10.1029/GM032p0099, URL http://doi.wiley.com/10.1029/GM032p0099.

Wang, X.J., Behrenfeld, M., Le Borgne, R., Murtugudde, R., Boss, E., 2009. Regulation of phytoplankton carbon to chlorophyll ratio by light, nutrients and temperature in the Equatorial Pacific Ocean: a basin-scale model. Biogeosciences 6 (3), 391–404. http://dx.doi.org/10.5194/bg-6-391-2009, URL https://bg.copernicus.org/articles/6/391/2009/.

Yacobi, Y.Z., Zohary, T., 2010. Carbon:chlorophyll a ratio, assimilation numbers and turnover times of Lake Kinneret phytoplankton. Hydrobiologia 639 (1), 185–196. http://dx.doi.org/10.1007/s10750-009-0023-3, URL http://link.springer.com/10.1007/s10750-009-0023-3.

Zhang, Q., 1999. Experimental study on the effect of salinity on growth rates of Arctic-sea-ice algae from the Greenland Sea. In: Gradinger, R., Spindler, M. (Eds.), Boreal Environ. Res. : Int. Interdiscipl. J. 04 (1), 1–8, URL https://oula.finna.fi/yliopisto/Record/arto.012447549.

Zhao, S., Cheng, W., Yuan, Y., Fan, Z., Zhang, J., Zhou, C., 2022. Global permafrost simulation and prediction from 2010 to 2100 under different climate scenarios. Environ. Model. Softw. 149, 105307. http://dx.doi.org/10.1016/j.envsoft.2022.105307, URL https://www.sciencedirect.com/science/article/pii/S1364815222000135.

Zienkiewicz, O.C., Taylor, R.L., Zhu, J.Z., 2013. The Finite Element Method: Its Basis and Fundamentals, Seventh ed. Elsevier, Butterworth-Heinemann, Amsterdam, OCLC: ocn852808496.